GREEN SYNTHESIS OF CELLULOSE GRAFT COPOLYMERS FOR ANION EXCHANGE WATER PURIFICATION

by

Stephen Christopher Schmal

A thesis submitted to the faculty of
The University of North Carolina at Charlotte
in partial fulfillment of the requirements
for the degree of Master of Science in
Chemistry

Charlotte

2022

Approved by:

_____
Dr. Jordan C. Poler

_____
Dr. Jerry M. Troutman

_____
Dr. Brian T. Cooper

_____
Dr. Donald Jacobs

ABSTRACT

STEPHEN C. SCHMAL. Green Synthesis of Cellulose Graft Copolymers for Anion
Exchange Water Purification. (Under the direction of DR. JORDAN C. POLER)

This thesis describes the synthesis and characterization of novel cellulose graft
copolymers that are used for the purification of drinking water. These nanomaterials
function as bottle-brush anion-exchange resins with repeating quaternary ammonium
polyelectrolyte chains covalently coupled to a cellulose scaffolding. In the synthesis
process of cellulose nanoresin (CNR), commercial microcrystalline cellulose is oxidized
at the C-6 position to form cellouronic acid via the (2,2,6,6-tetramethylpiperidin-1-
yl)oxidanyl (TEMPO) radical while under sonication, or high-pressure homogenization.
Polyelectrolyte chains are then synthesized with controlled strand lengths using the
ARGET-ATRP mechanism. CNR was prepared in all-aqueous medium by Fischer-Speier
esterification using a catalytic amount of hydrochloric acid. Carboxyl contents of
TEMPO-oxidized nanocellulose (TONC) and of CNR were measured using
conductometric titration, with values as high as 1.61 mmol g^{-1} for TONC and as low as
0.627 mmol g^{-1} for CNR respectively. Percent functionalization of CNR was calculated to
be 61%. The hydrodynamic diameter and zeta potential of TONC and CNR were
measured by dynamic light scattering (DLS). DLS data showed a decrease in the size of
the particles in dispersion after the oxidation of cellulose. Consistent with our graft
copolymer model, the particle's size increased after polyelectrolyte functionalization. The

surface charge of dispersed particles of commercial cellulose, TONC, and CNR also changed from neutral to negative to positive at pH 7, indicating successful synthetic procedures. CNR was further characterized by testing its functionality as a thin-film membrane and as an adsorbent material for anion exchange applications. CNR membranes were found to exhibit high water flux of >700 L m^{-2} h^{-1} bar^{-1} and high loading capacities of >20 mg g^{-1} when tested using a sodium fluorescein (NaFL) surrogate adsorbate. These materials exhibit fast kinetics, with equilibrium loading being achieved in a matter of seconds. CNR thin films are regenerable and reusable as water purification membranes, with a decrease in loading capacity of only 0.01 ± 0.01 mg NaFL per gram of CNR, or 0.03% after 40 cycles.

ACKNOWLEDGEMENTS

I would like to first thank Dr. Jordan C. Poler for his unyielding commitment to my education. His willingness and eagerness to work with me and guide my understanding of his lab's work has allowed me to strengthen my research skills and my ability to complete and explain lab-based projects. He has worked diligently and relentlessly to make sure that I have had all of the resources and opportunities that I could possibly need, and for that I will be forever grateful. Second, I would like to thank Dr. Abhispa Sahu for her essential contributions to this project and for laying the groundwork for my research in Dr. Poler's lab. I am so thankful for her willingness to be available for assistance with technical questions even after graduating from UNCC. I would also like to express my gratitude for all of the contributions that have been made and are continuing to be made by the Poler Research Group to the water purification project, specifically those I have had the pleasure with working alongside including Sydney Elmore, Abby Oliver, Terwait (Art) Kongruengkit, Christopher Reid, Jenna Costelloe, Rachel Rollins, Jenna Barilovits, Nikki Thai, Raghav Dosi, and Carly Kwiatkowski. I would like to thank Dr. Jon Merkert, Dr. Adam Fessler and Varsha Godakhindi for the time that they took out of their busy schedules to train me on various lab instrumentation. Lastly, I would like to personally thank Dr. Thomas D. Walsh for financial contributions to my education through the Thomas D. Walsh Tuition Fellowship and to the EPA P3 Grant and NSF Ventureprise funding for partial support of my researc

TABLE OF CONTENTS

LIST OF TABLES

LIST OF FIGURES

LIST OF ABBREVIATIONS

ADP	Adenosine diphosphate
AGU	anhydroglucose unit
AMP	Adenosine monophosphate
ARGET-ATRP	Activators regenerated by electron transfer atom transfer radical polymerization
ATP	Adenosine triphosphate
ATRP	Atom transfer radical polymerization
CC	Carboxyl content
^{13}C NMR	Carbon-13 nuclear magnetic resonance spectroscopy
CNR	Cellulose nanoresin
DBPs	Disinfection byproducts
DLS	Dynamic light scattering
DMF	Dimethyl formamide
^{1}H NMR	Proton magnetic resonance spectroscopy
HEBIB	2-hydroxyethyl 2-bromoisobutyrate
ITC	Isothermal titration calorimetry
NaFL	Fluorescein disodium salt
PF	Percent functionalization
PFAS	Per- and polyfluoroalkylated substances
Poly (vbTMAC)	Poly (vinyl benzyl trimethyl ammonium chloride)
PPE	Polypropylene
RNase A	Ribonuclease A (from bovine pancreas)

SI-ATRP	Surface-initiated atom transfer radical polymerization
TEMPO	2,2,6,6-tetramethylpiperidin-1-yl)oxidanyl
TONC	TEMPO-oxidized nanocellulose
TPMA	Tris(2-pyridylmethyl)amine
USEPA	United States Environmental Protection Agency

CHAPTER 1: INTRODUCTION

1.1 Background on Cellulose and Cellulose Derivatives

Cellulose and its derivatives have been used for a wide variety of applications including wastewater treatment,[1] coatings, and tissue engineering.[2] The scope of cellulose applications has been extended by various surface modifications of cellulose nanofibrils. Cellulose modification reactions typically consist of esterification or etherification reactions. Cellulose ethers have been used as stable thickeners in the form of carboxymethylcellulose,[3, 4] methylcellulose,[5] and hydroxyethyl- and hydroxypropyl-cellulose.[3, 6] Cellulose esterification can be used to introduce a wide range of organic moieties to the polymer chain, allowing for versatile chemical modification. Cellulose esters have been synthesized mainly by inorganic esterification,[7] Fischer-Speier esterification,[8] mechanochemical esterification,[9] and transesterification[10] of nanocelluloses. Esterification of nanocelluloses has been achieved without the use of additional solvents, using esterification agents such as citric[11] and sulfuric acid.[12] These all-aqueous syntheses lay the groundwork for the acid-catalyzed, all-aqueous synthesis of sustainable cellulose-based water purification materials.

Cellulose esters such as cellulose di- and triacetate[13] and cellulose nitrate[14] are typically used as functional films or fibers.[15] Chemical modifications to cellulose have also been used to study its performance as a scaffold for ion-exchange materials.[16] Crosslinking[17] and polymer blending of cellulose acetate and poly(methyl methacrylate)[18] have been studied to increase the ion exchange capacity of polymer blends, with proton conductivities on the order of 10^{-2} and 10^{-3} S cm^{-1}, respectively. Described in this thesis

is the synthesis of cellulose-scaffolded graft copolymers with covalently bonded polyelectrolyte branches for use as ion-exchange water purification materials.

1.2 Cellulose Esterification

Cellulose, the most abundant biopolymer, contains three hydroxyl groups per anhydroglucose unit (AGU). These are the secondary hydroxyl groups at the C-2 and C-3 positions and the primary hydroxyl group at the C-6 position. All of these groups are capable of participating in alcoholic hydroxyl group reactions including esterification, etherification, and oxidation.[19] In esterification reactions of cellulose, homogeneous and heterogeneous esterification can be applied, to either modify the whole polymer chain or to modify only the surface of the cellulose fibers.[20] Cellulose esterification can be used to introduce a wide range of moieties to the polymer chain, allowing for versatile chemical modification. During the esterification of nanocellulose, the main the challenge is to conduct the reaction in such a way that the structural integrity of the crystalline cellulose interior is maintained, while esterification mainly occurs on the hydroxyl groups on the surface of the nanocellulose.[21] Fischer-Speier esterification has been extensively applied to cellulose, specifically for the single-step isolation of surface-functionalized nanocellulose. This acid-catalyzed esterification process typically involves the use of an organic acid reagent such as acetic, butanoic, citric, malic, or malonic acid.[22] Hydronium ions produced by dissociation of hydrochloric acid hydrolyze amorphous cellulose domains and catalyze the esterification of cellulose hydroxyl groups. This method has been reported to produce stable nanocellulose dispersions in organic solvents. In this

thesis, we report the development of an all-aqueous process for the esterification of surface-modified nanocellulose.

1.3 TEMPO-mediated cellulose oxidation

As previously mentioned, the C-2, C-3, and C-6 hydroxyl groups of cellulose are capable of classic alcoholic reactions, such as oxidation. The breadth of nanocellulose functionality can therefore be increased by oxidation of these groups to aldehyde, ketone and carboxyl groups. One such method that has been extensively studied is 2,2,6,6-tetramethylpiperidine-1-oxyl (TEMPO)-mediated oxidation. TEMPO-mediated oxidized nanocellulose (TONC) has gained attention for its applications in polyelectrolyte and intermediate synthesis. During this process, the stable aminoxyl radical in TEMPO is oxidized by NaClO to the N-oxoammonium ion (figure 1), which then rapidly oxidizes the primary C-6 hydroxyl groups of cellulose to carboxyl groups through C6-aldehyde

intermediates.[15] In the final step of this mechanism, NaBrO (formed from the oxidation of NaBr) oxidizes the N-hydroxy-TEMPO to propagate the reaction. A similar approach
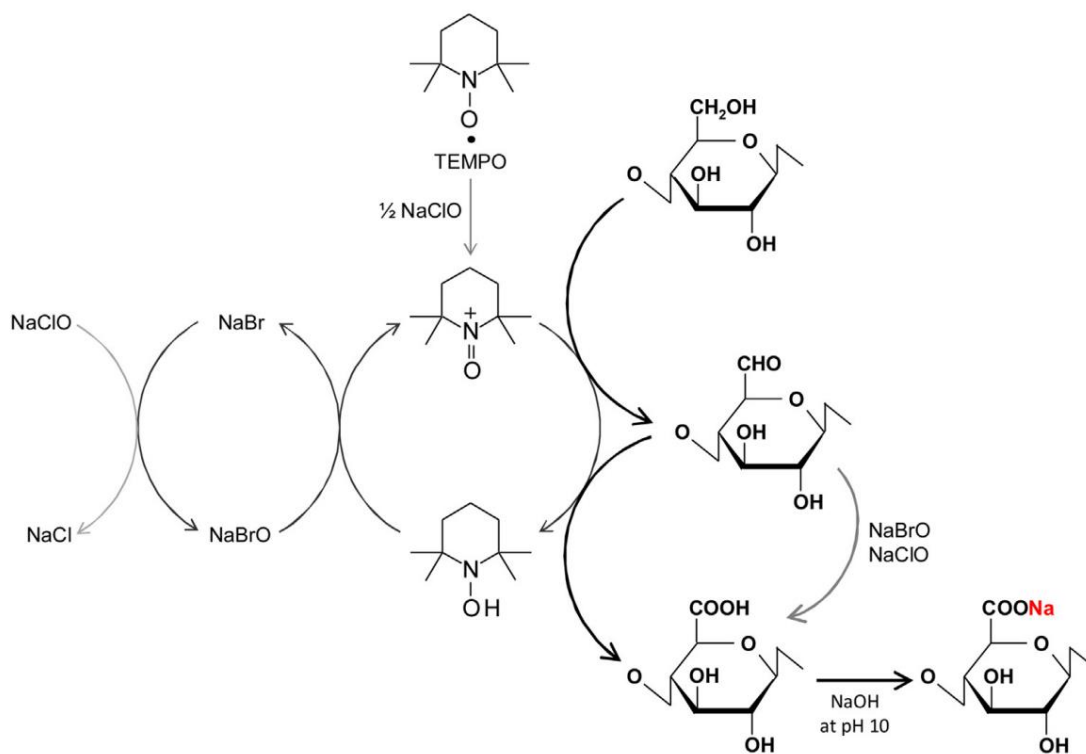
Figure 1: Selective C6 oxidation of primary hydroxyl groups of cellulose by the TEMPO radical in pH basic conditions. Used without permission Isogai et al.

to this reaction was performed by Saito *et al.* by stirring cellulose, TEMPO, and $NaClO_2$ in a 0.05 M sodium phosphate buffer in a reaction flask at 500 RPM at 60 °C for 2-72 hours.[23] In this TEMPO/NaClO/$NaClO_2$ system, the NaClO oxidizes the N-hydroxy-TEMPO. The study notes the importance of pH, with efficient oxidation being observed at pH 6.8, and nearly no carboxyl groups being formed at pH 3.5. X-ray diffraction and ^{13}C NMR analyses revealed that TEMPO selectively oxidized the primary C-6 hydroxyl groups on the fibril surfaces to carboxyl groups.

1.4 A Review of Aqueous Cellulose Esterification

   In the esterification methods mentioned above, several applications of the

produced nanomaterials are hindered due limitations of these procedures. These

limitations include the use of organic solvents, harsh reaction conditions, and

complicated preparation procedures. Aqueous cellulose esterification has been studied as

an alternative route to avoid these limitations. Chen *et al.* reported the alkaline aqueous

esterification of cellulose for thiol-ene click reaction functionality.[24] Using a

water/sodium carbonate solvent, methacrylic anhydride as an esterification agent was

used to produce methacrylated cellulose (figure 2). The reaction was carried out at room

temperature for 12 hours, centrifuged to remove the cellulose, washed with DI water and

methanol, and dried in vacuum for 24 hours at 40 °C. FTIR spectra showed a new peak
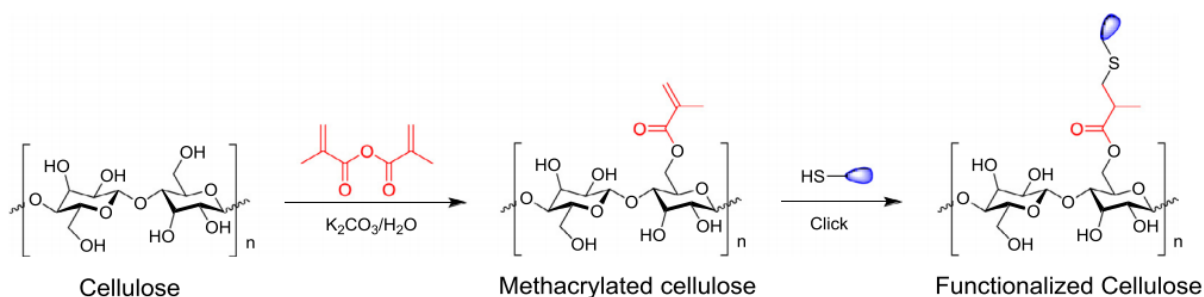
Figure 2: Aqueous cellulose esterification. Methacrylated cellulose by methacrylic anhydride esterifying agent and thiol-ene click functionalization. Used without permission Chen et al.

in methacrylated cellulose at 1720 cm^{-1}, indicating the presence of carbonyl groups.

Cross-Polarization Magic Angle Spinning Carbon-13 Nuclear Magnetic Resonance

spectroscopy revealed three new peaks after methacrylation, corresponding to the methyl,

vinyl, and carbonyl groups. XRD analysis showed that esterification in alkaline solution

had no significant influence on the crystal structure of cellulose, indicating that

esterification largely occurred in the amorphous domains of the cellulose. While their

study focused on the proposal of thiol-ene click functionalization, it must also be noted that the alkene group of the methacrylated cellulose might also exhibit polymerization functionality to produce copolymer species via ATRP.

1.5 Cellulosic cation-exchange materials

The increase in cation ion-exchange capabilities by surface modification of cellulose has been achieved by sulfonation[25] and phosphorylation[26] for the adsorption of Cu^{2+} and Ni^{2+}, Fe^{2+}, and UO_2^{2+}. Quaternization[27] of cellulose has also been studied for the synthesis of anion-exchange materials for the removal of Cr(VI) in the form of chromate, hydrogen chromate and dichromate. Isogai's work on site-specific oxidation of the primary hydroxyl in cellulose using TEMPO has enabled a facile click-like methodology for cellulose modification.[28] The synthesis of polyglucouronic acid, or cellouronic acid, has led to applications in flexible electrodes,[29] antistatic coatings, electrical conductors,[30] energy storage,[31] and ion-exchange membranes.[32, 33] Cellouronic acid is a commonly used support material for nanofiltration ion-exchange membranes produced by interfacial polymerization of monomer building blocks.[34] Modified cellulosic materials have been used to produce cation-exchange membranes for the removal of heavy metals such as lead, copper, zinc, nickel, cobalt, cadmium, mercury, iron, and chromium.[16, 35]

Cellulosic ion-exchange membranes and resins have been extensively studied for applications in water purification technologies. Currently, most nanofiltration membranes are produced by interfacial polymerization of monomer building blocks, with cellulose acetate being a commonly used support material.[34] Cellulose-based copolymer brushes as

polymeric membrane adsorbents have been synthesized using Surface-Initiated Atom

Transfer Radical Polymerization (SI-ATRP). Singh *et al.* achieved surface

functionalization of poly (acrylic acid) (PAA) onto regenerated cellulose (RC)

membranes. The reaction of 2-bromoisobutyryl bromide ATRP initiator with the

hydroxyl groups of the RC membrane allowed for covalent functionalization of weak

cation-exchange groups onto the membrane surface.[36] ATR-FTIR spectroscopy was used

to support the successful grafting of PAA from the membrane surface. The appearance

of peaks at 1560 and 1416 cm^{-1} indicated carboxylate anion stretching in polymer-

modified membranes.

1.6 Cellulose graft copolymers

      SI-ATRP has been used to synthesize graft copolymer brushes from cellulose

nanofibers. Morits *et al.* synthesized copolymer brushes (figure 3) by functionalization

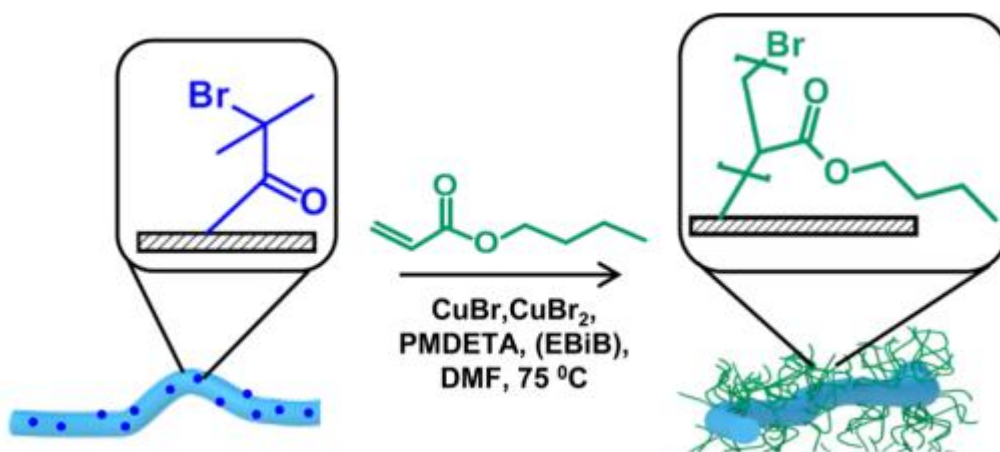of CNF with poly(n-butyl acrylate) (PnBA) and poly(2-(dimethyl amino)ethyl

Figure 3: SI-ATRP from CNF-Br in the presence of EBiB, for n-butyl acrylate (nBA).
Used without permission Morits et al.

methacrylate) (PDMAEMA).[37] This study found that increasing the degree of

substitution led to a noticeable fragmentation of CNF after polymerization. Morits *et al.* suggested that degradation of the disordered CNF domains was caused by side-chain brush strain. Therefore, a careful balance must be considered in avoiding excessive degradation and achieving high grafting density. Reported kinetics of SI-ATRP for PDMAEMA and PnBA grafting were first order and pseudo-first order, respectively. FT-IR and ^{1}H NMR were used to show successful grafting of polymer brushes.

Cellulose-based nanomaterials have been synthesized from reaction of oxidized cellulose with primary hydroxyl-bearing species. This method has been used to graft copolymers similar to those described in the previous section. Shown in figure 4, S. Nematdoust *et al.* synthesized the graft copolymer Cell-g-mPEG via Fischer-Speier esterification.[38] To achieve the desired oxidized cellulose, sonication of natural cellulose
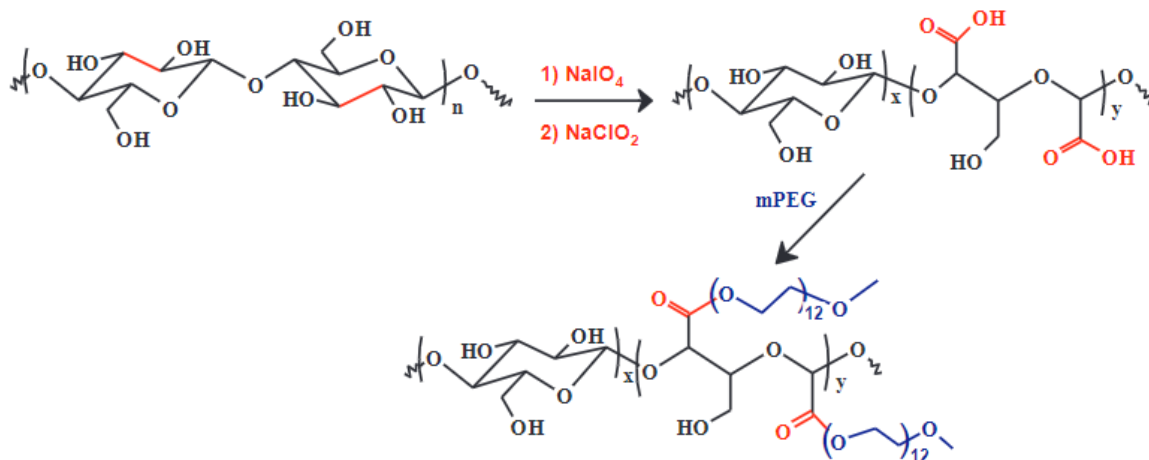
Figure 4: Fischer-Speier Esterification of dicarboxylated cellulose for synthesis of graft copolymer Cell-g-mPEG. Used without permission Nematdoust et al.

was applied for three hours before reaction with $NaIO_4$ to produce 2,3-dialdehyde cellulose. The cellulose aldehyde product was then reacted with $NaClO_2$ to produce 2,3-dicarboxylic acid cellulose. Introduction of dicarboxyl groups, as well the cleavage of the C2-C3 bond was confirmed by ^{13}C NMR spectroscopy. The graft copolymer Cell-g-

mPEG was synthesized by grafting poly(ethylene glycol) monometheyl ether (mPEG) to the oxidized cellulose backbone. Fischer-Speier esterification was catalyzed by p-toluenesulfonic acid in a toluene solvent.
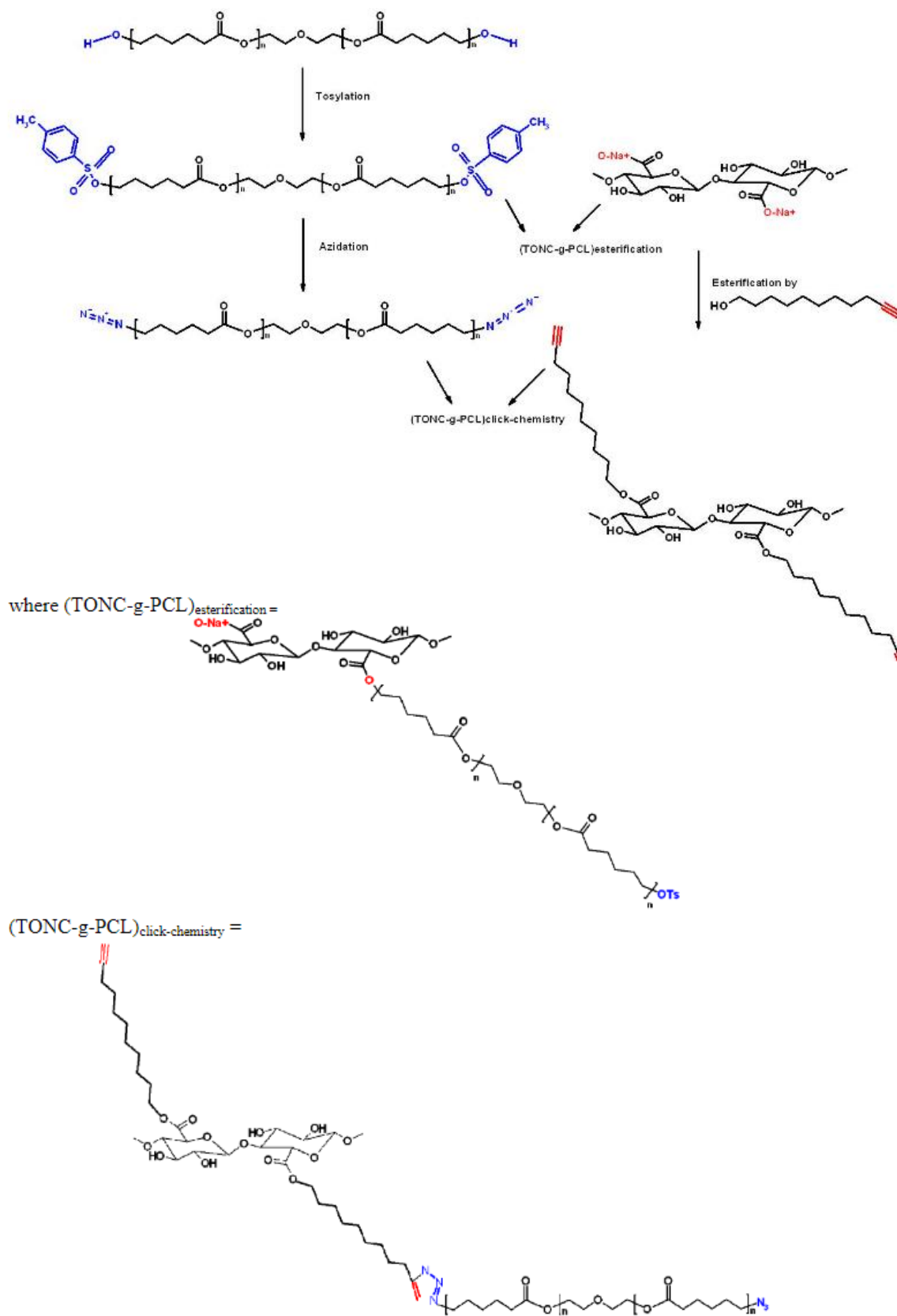
Figure 5: Grafting of polycaprolactone-diol onto TONC by direct esterification and click chemistry. Used without permission Benkaddour et al.

In a similar study, TONC was used as a backbone for the synthesis of graft copolymers with polycaprolactone-diol (PCL) side chains.[39] In this study, both click-chemistry and esterification were evaluated as surface modification treatments to improve the dispersion of nanofibers in organic media. Both strategies are depicted in figure 5. In the esterification strategy, the copolymer was grafted by reacting the hydroxyl groups of PCL and the carboxyl groups of TONC. It is noted that the grafting of PCL by esterification did not exceed 5% w/w, due to the large molecular weight of PCL, which induced steric hindrance and thus affected the grafting density. The alternative click-chemistry method was introduced as a solution to the low grafting densities produced by esterification. In this strategy, the 1,3-dipolar cycloaddition reaction between azides and terminal alkynes was applied for grafting the copolymer species.

1.7 Cellulose graft copolymers with anion exchange functionality

Oxidized cellulose structures have been used to synthesize copolymers with applications in ion-exchange membranes. Singh *et al.* achieved surface functionalization of poly (acrylic acid) onto regenerated cellulose membranes.[36] Cellulose nanofiber modification by surface-initiated atom transfer radical polymerization has been used to graft copolymer brushes that have applications in binding and separation of biomolecules, microelectronics, and ultrafiltration.[37] Though the grafting of cellulose-polyelectrolyte copolymers has been studied, the synthesis of a copolymer using the carboxyl functional groups of TEMPO-oxidized nanocellulose (TONC) and the primary alcohol of an atom transfer radical polymerization (ATRP) initiator is a novel synthesis. Reported in this thesis is the acid-catalyzed Fischer-Speier esterification using the carboxylated groups of

TONC and the primary alcohol group of the 2-hydroxyethyl 2-bromo-isobutyrate (HEBIB) ATRP initiator to produce a graft bottle-brush copolymer. These materials exhibit anion-exchange functionality with potential applications in water purification as thin film membranes.

CHAPTER 2: MATERIALS AND METHODS

2.1 Poly (vbTMAC) synthesis

Poly(vinyl benzyl trimethyl ammonium chloride) (poly(vbTMAC)) was

synthesized via the activators regenerated by electron transfer atom transfer radical

polymerization (ARGET-ATRP) method, originally developed by Matyjaszewski *et al.*[40]

The catalyst was prepared by adding 51.7 µL of a 20.6 mM copper (II) bromide (1.07

µmol) (Arcos, 99+%; Lot #A0344238) solution to 1.000 mL water along with 18.50 mg

(63.71 µmol)of tris(2-pyridylmethyl)amine (TPMA) (TCI, >98.0%; Lot #Z8GMO-A).

The monomer vinyl benzyl trimethyl ammonium chloride (vbTMAC) (Fisher, 97%;

Lot#A0311318) (1.6001 g, 7.557 mmol) was added to 30.0 mL of DI water. The mixture

was then sparged with Ar(g) for 20 minutes to remove oxygen from the reaction vessel,

as oxygen would oxidize the copper in the catalyst complex from the Cu^+ to the Cu^{2+}

state, thereby removing the activator species from the reaction. The ATRP initiator

HEBIB (Sigma-Aldrich, 95%, Lot #MKBW2607) was then added (35.5 µL, 252 µmol).

The reducing agent, tin(II) 2-ethylhexanoate (Sigma-Aldrich, 92.5–100%, Lot

#SLBP5072V) was then added to the reaction vessel (60 µL). The reaction vessel was

heated in a 110 °C oil bath with constant stirring under Ar(g) at reflux conditions for 151

h. Using vacuum evaporation, the solvent was removed from the purified polymer

solution. This mass from a known volume was used to determine the concentration of

poly(vbTMAC), which was found to be 10-100 mg/mL.

Several 100 µL aliquots were taken during the reaction for 1H NMR analysis to

quantitatively measure the percent conversion of vbTMAC monomer to polymer.

Percent conversion was measured by integrating the doublet at 5.8 ppm chemical shift,

which corresponds to the vinylic proton H_{1a} (see figure 7). Dimethyl formamide was added as an internal standard (10.00 µL) and each aliquot was diluted by a factor of 10 into D_2O and filtered using 0.45 µm pore size nylon Cameo 3N syringe filters (GE Water & Process Technologies, Catalog No. DDR0400300). Figures 7 and 8 show the ^{1}H NMR spectra of the vbTMAC monomer and the polymerized product, respectively. Percent conversion was calculated as $Percent\ Conversion = \left[1 - \left(\frac{S_t}{S_0}\right)\right] * 100\%$ where S_t is the integrated signal at 5.8 ppm of the vinylic proton on the vbTMAC monomer at time t and S_0 is the integrated signal at the start of the polymerization. Once 99% conversion was achieved, the reaction was quenched by allowing air into the reaction vessel and the product was purified by centrifuging at 15,000 RCF for 4 h and then dialyzing against water through a 2 kDa molecular weight cut off cellulose dialysis membrane to remove any remaining monomer and other reagents. Reaction kinetics were analyzed by plotting the natural logarithm of the initial concentration of vbTMAC monomer, $[M]_0$ over the concentration at time t, $[M]_t$ as a function of reaction time in hours. The slope of this line was then used to determine the reaction's rate constant. Shown in figure 6, the polymerization followed psuedo-first order kinetics with a rate constant of 1.6 x 10^{-2} h^{-1}.
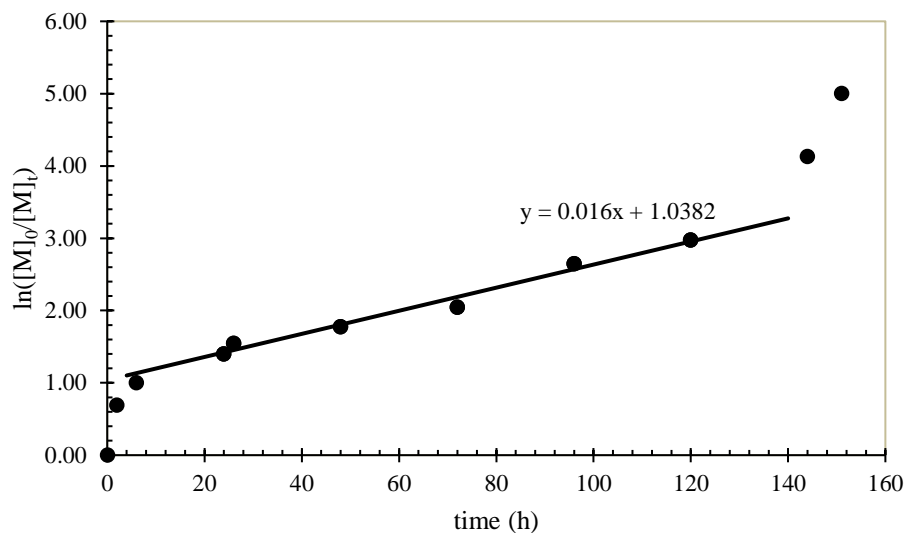
Figure 6: vbTMAC polymerization kinetics. Reaction proceeded with pseudo-first order kinetics, with a rate constant of 1.6×10^{-2} h^{-1}.

As mentioned in Sahu 2020, the rate of ARGET ATRP of poly (vbTMAC) can be increased with sonication, with a reported rate constant of $k_{app} = 3.2 \times 10^{-3}$ s^{-1} when using sonic irradiation of 125 W cm^{-2} at 19.5 °C bulk temperature.
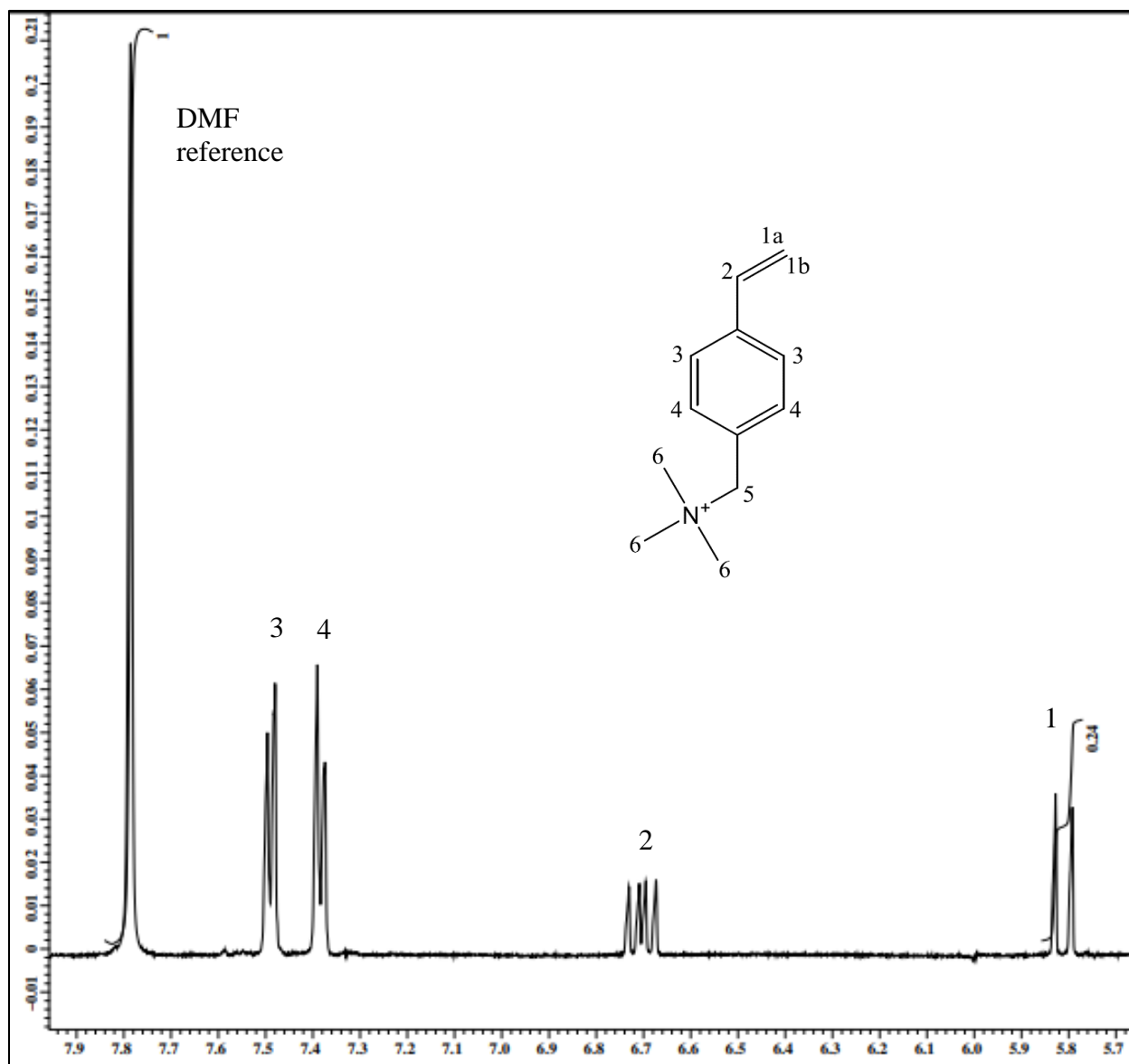
Figure 7: ^{1}H NMR spectrum of vbTMAC monomer using DMF internal standard. Vinylic protons at 5.8 ppm showed an integrated signal of 0.24 before polymerization was initiated.
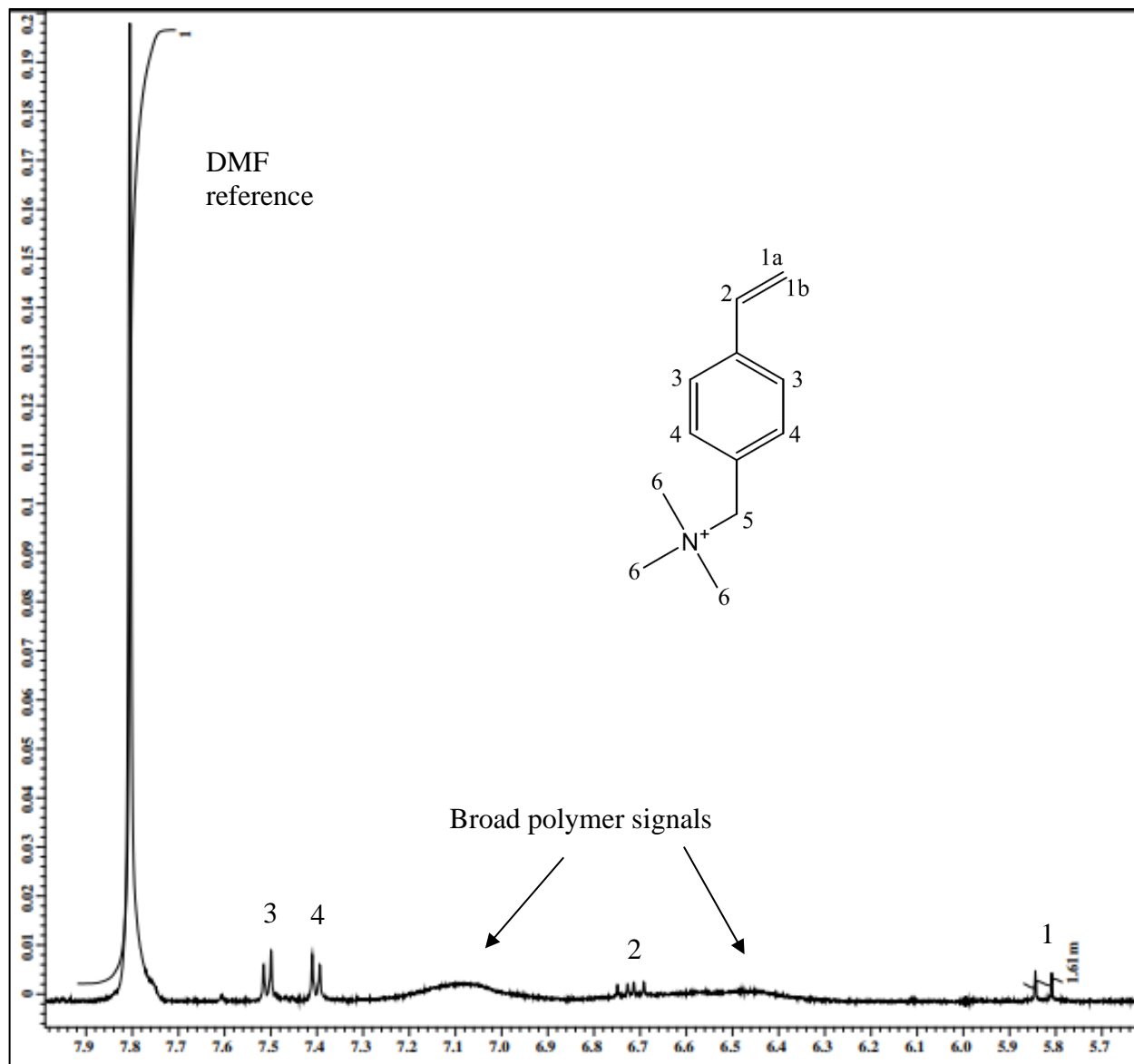
Figure 8: ^{1}H NMR spectrum of poly(vbTMAC) after 151 h of reflux. Vinylic protons at 5.8 ppm showed an integrated signal of 0.00161, indicating a percent conversion of 99%.

2.2 TEMPO-mediated C-6 carboxylation of cellulose

2.2.1   Oxidation of cellulose was performed using 2,2,6,6-tetramethylpiperidine 1-oxyl (TEMPO) (Sigma-Aldrich, Lot #BCBZ3312). This procedure made use of the well-established synthetic route that selectively targets the C-6 carbon of the D-glucose monosaccharide units.[33] In a 50 mL round bottom flask, NaBr (Fischer Scientific, Lot

#067787) (0.256 g, 2.49 mmol) and TEMPO (11.64 mg, 74.5 µmol) were dissolved in

25.0 mL of water. Cellulose (Sigma-Aldrich, Lot# MKCJ3230) (0.512 g, 3.16 mmol of

glucose monomer) was then added, and the pH was adjusted to 10.3 using a standardized

solution of 189.3 mM NaOH. Oxidation was initiated by adding 8.5 mL (13.9 mmol) of

NaOCl while maintaining the pH using NaOH. The reaction mixture was cooled to 10

°C using an RTE-9 Endocal refrigerated cooling bath and sonicated at 72 W cm^{-2} to

debundle the cellulose fibers. Sonication was stopped after 2 hours, the sonicating probe

was removed, and the reaction was capped and stirred for 24 hours at 10 °C. Ethanol was

added to the reaction vessel to quench the oxidation, and the products were centrifuged

with ethanol twice and acetone once at 15,000 g at 4 °C for 1 hour each. Following each

centrifugation, the supernatant liquid was discarded, and the pellet was scraped out. The

pellet from the final washing was dried for 24 hours in a vacuum oven at 90 °C. The

dried pellet was dispersed into 100.0 mL of water and sonicated at 45 W cm^{-2} for 20

minutes. The dispersion was then centrifuged at 100,000 g at 20 °C for 75 minutes and

the supernatant containing the TEMPO-oxidized nanocellulose (TONC) product was

collected. The concentration of TONC was determined by solvent evaporation to be 96

mg/L.

2.2.1 Carboxylate content of oxidized cellulose

Carboxyl content of cellulose was determined by conductometric titration. In this

experiment, the TONC sample is prepared in excess 0.1 M HCl and then titrated with

NaOH. As NaOH is added to the mixture, the conductivity decreases rapidly (figure 9)

due to the fast-moving H$^+$ ions being removed from the solution and replaced by larger,

and therefore slower Na^+ ions. Once sufficient NaOH is added such that the HCl is neutralized, the NaOH begins deprotonating the carboxyl groups of TONC. During this process, the weak carboxylic acid groups of TONC in the mixture are replaced by highly soluble $-RCOO^-Na^+$ groups, which slowly drives the conductivity upward. Upon the addition of enough NaOH to deprotonate all of the carboxyl groups in the TONC, the addition of excess NaOH introduces more ions to the solution, which causes the conductivity to increase rapidly.

In this experiment, 10.000 mL of dispersed TONC was added to 100.0 mL of water and 1.000 mL of 0.1 M HCl to reduce the pH far below the pKa of acetic acid, ensuring the protonation of all C-6 carboxyl groups in TONC. The initial pH of the solution was 1.29. A standardized solution of NaOH (189.3 mM) was added 1.000 μL at a time, and the conductivity was monitored using a conductivity probe (Fischer Scientific, AR20 pH/conductivity meter with Acumet Research conductivity probe). The conductivity of the mixture was measured at each 1 μL interval and was then plotted as a function of the volume of NaOH added. Linear regression analysis was used to plot three straight lines through the linear portions of the graph, shown as lines 1, 2, and 3 in figure 9. The volume of NaOH required to neutralize the carboxyl groups of TONC was determined by subtracting the volume at which lines 1 and 2 intersect, V_1 from the volume at which lines 2 and 3 intersect, V_2. Carboxyl content of TONC was calculated by dividing the number of moles of NaOH required to deprotonate the carboxyl groups of TONC by the mass of TONC.
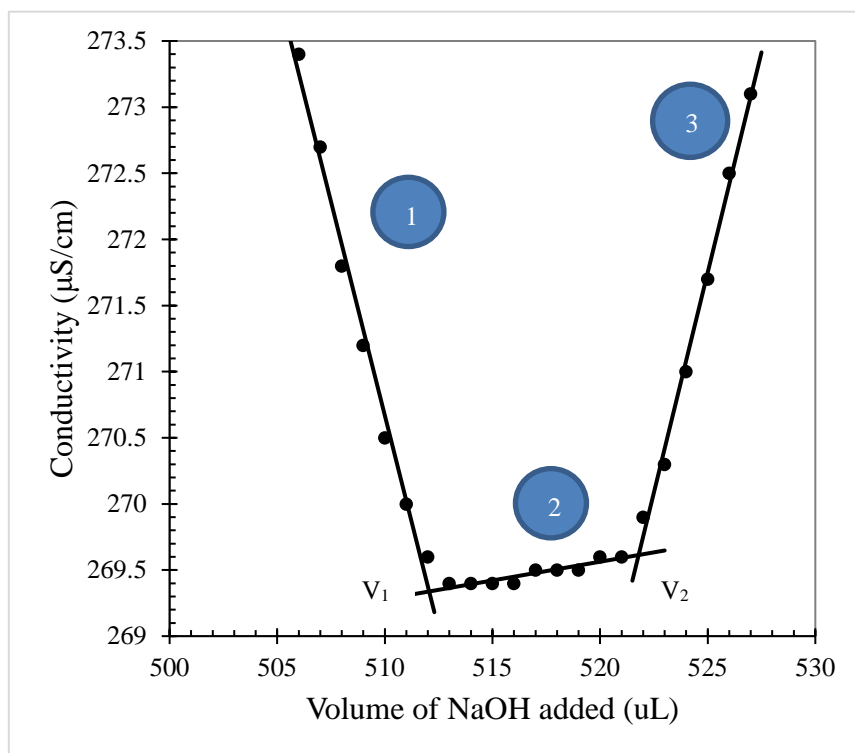
Figure 9: Example conductometric titration of TONC.

2.3 Cellulose nanoresin synthesis

Poly(vbTMAC) and TONC were coupled via acid-catalyzed Fischer-Speier esterification (figure 10). The two polymers were added to a 50 mL round bottom flask and refluxed for 72 hours. 5.000 mL of poly(vbTMAC) (estimated to be ~21 kDa, 9.149 µmol) and 17.000 mL of TONC (96 mg L^{-1}, 1.6 µmol g^{-1}, 2.6 µmol of TONC carboxyl groups) were mixed with 200 µL of concentrated HCl. The pH of the reaction mixture was measured to be 2.23. After 72 hours of reflux, the reaction was quenched, and the coupled product was collected. The product was then filtered using 0.2 micron pore size, 13 mm poly(propylene) membrane filters (Sterlitech, Lot #18103-008-002) to remove any unreacted polymer. Following the esterification reaction, conductometric titration
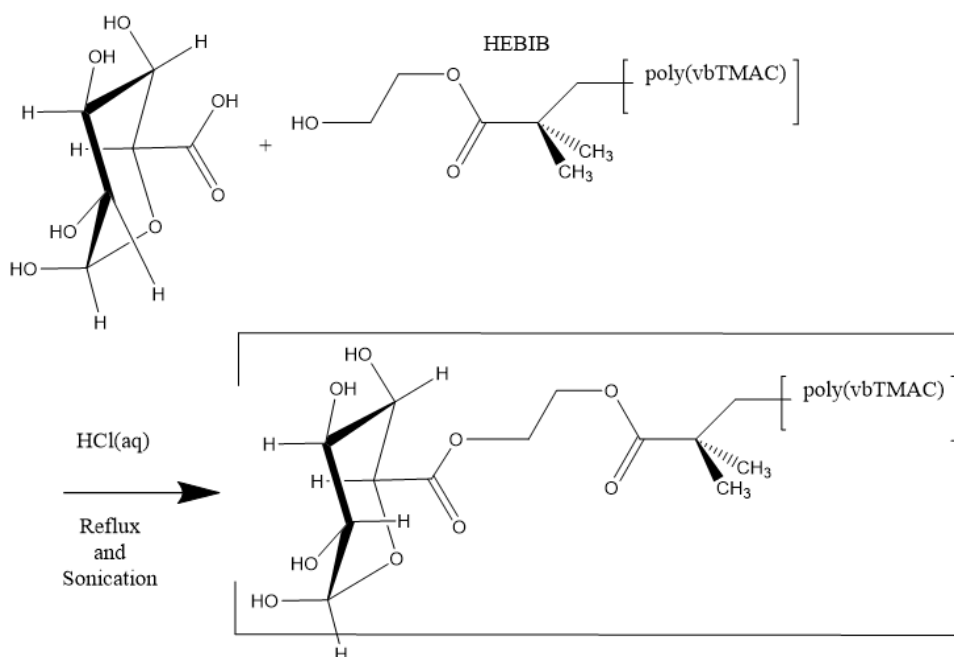
Figure 10: Coupling of poly (vbTMAC) to TONC via hydrochloric acid-catalyzed Fischer-Speier esterification. HEBIB initiator is coupled to the carboxyl group of TONC by reaction with its primary hydroxyl group.

was used to determine the percent functionalization of the cellulose nanoresin (CNR). During the titration, 0.1893 M NaOH was added to 10.000 mL of 96 mg/L CNR product. Percent functionalization (PF) was calculated as $PF = 100 - \left[\frac{CC_E}{CC_0} * 100\right]$ where CC_E is the carboxylate content of the esterification product and CC_0 is the carboxylate content of the original TONC.

CNR synthesis was optimized by first experimenting with alternative synthetic methods for TONC synthesis. High-pressure homogenization was used during the oxidation reaction to increase the surface area of the cellulose reagent. For this reaction, 20.0048 g cellulose was added to 2.000 L of DI water and 9.8563 g NaBr was dissolved in the mixture. 20.0 mL of 171.8 mM NaOH was then added, and the pH was measured

to be approximately 10 using Carolina universal indicator strips. 450 mg of TEMPO was then added to the reaction mixture, and 175 mL of 8.25% NaClO was then introduced to allow oxidation to begin. The reaction mixture was passed through the high-pressure homogenizer 12 times at 8,000 PSI, then 4 more times at 14,000 PSI. The HPH TONC was then centrifuged and purified using ethanol and acetone as described above. A second sample of TONC was prepared by sonicating HPH TONC for 2 h at 10 Wrms before centrifuging and purifying the sample. A third TONC sample was prepared by sonication only, while measuring the pH of the reaction mixture during the oxidation reaction. For this reaction, 1.023 g cellulose was added to 50.0 mL DI water along with 514.1 mg NaBr and 23.6 mg TEMPO. 500 μL of 171.8 mM NaOH was then added and the pH was measured to be 10.19. The reaction was started by adding 17.0 mL of bleach, after which the pH was measured to be about 4 using universal indicator strips. 6.000 mL of 171.8 mM NaOH was then added, and the pH was measured to be approximately 10. The pH of the reaction was measured every 15 minutes for 2 h and did not change for the entirety of the reaction. The reaction mixture was sonicated for 2 h at 10 Wrms before subsequent quenching and purification. The carboxylate content of the three TONC samples (HPH only, HPH + sonicated, and sonicated, pH controlled TONC) were measured by conductometric titration. As shown in figure 11, the neutralization of the acetate groups in 10 mL each of HPH only, HPH + sonicated, and sonicated, pH controlled TONC required 8 μL, 10 μL, and 18 μL of 171.8 mM NaOH, giving carboxylate contents of 1.13 mmol g^{-1}, 1.26 mmol g^{-1} and 1.61 mmol g^{-1}, respectively. For subsequent CNR synthesis esterification reactions, the TONC sample with the highest carboxylate content - sonicated, pH controlled TONC - was used.
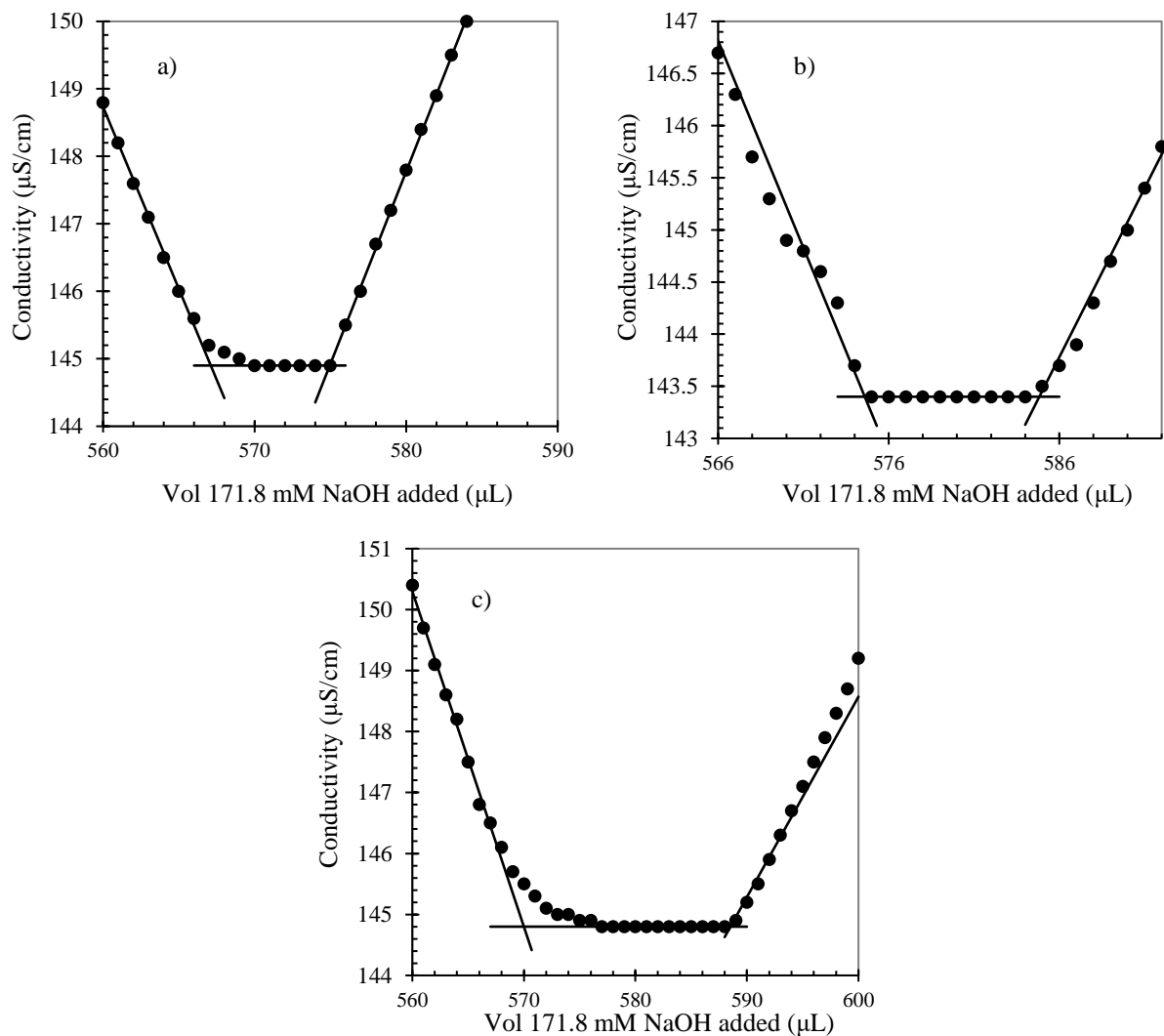
Figure 11: Conductometric titration of 10 mL each of HPH only (a), HPH + sonicated (b), and sonicated, pH controlled TONC (c). Neutralization of acetate groups required 8 μL, 10 μL, and 18 μL of 171.8 mM NaOH, respectively. Carboxylate contents for these TONC samples were calculated to be 1.13, 1.26, and 1.61 mmol g^{-1}, respectively.

Esterification of sonicated, pH controlled TONC was carried out four times with varying mole fractions to determine the stoichiometry of the reaction. Each reaction was performed under reflux conditions for 72 h using 10.000 mL of 192 mg L^{-1} TONC and 100.0 μL concentrated HCl. The carboxylate content of sonicated, pH controlled TONC was determined by conductometric titration to be 1.61 mmol/g (figure 11). Poly(vbTMAC) 30-mer, (14.8 mg mL^{-1}, estimated molar mass = 6563 Da) was added using volumes of 137.0 μL, 685.0 μL, 1.370 mL, and 2.740 mL to reach mole fractions of 0.1, 0.5, 1, and 2, respectively. Following the completion of the esterification reactions, each product was filtered with 0.2-micron pore size, 13 mm polypropylene filters. PF was then determined for each product using conductometric titration. During each titration, 2 mL of CNR was mixed with 100 mL of water and 2 mL of 0.1 N HCl and then titrated with 17.18 mM NaOH. Carboxylate content of each product was calculated from the moles of NaOH required to neutralize the carboxyl groups, and PF was calculated.

TONC Esterification reaction time was varied over six iterations. For each reaction, 5.000 mL of 192 mg/L TONC was added to 1.370 mL poly(vbTMAC) 30-mer (14.8 mg/mL) along with 100.0 μL concentrated HCl. Reaction times of 1 h, 4 h, 6 h, 14 h, 17 h, and 24 h were performed and characterized. PF for each reaction was determined by conductometric titration and the reaction time which produced the highest carboxyl content was 17 h. Using DLS analysis, a maximum particle size and a positive surface charge were also observed when the reaction was allowed 17 h reflux.

2.4 CNR as anion-exchange materials

The adsorption capacity of CNR was determined using UV-Vis spectroscopy.

Fluorescein disodium salt (NaFL) (Sigma-Aldrich Lot #: BCBR1213V, CAS: 518-47-8)

was used as a surrogate adsorbate for natural organic matter acids. Fluorescein, FL

speciates into three forms – FL, FL^- and FL^{2-}. During incubation with CNR, all species

are adsorbed, but at neutral pH, most of the fluorescein is in the FL^- state. Once sufficient

incubation time had passed to reach equilibrium, the effluent was filtered using 0.45 μm

pore size nylon filters and the pH was increased to >11 to deprotonate all FL in the vial,

leaving only FL^{2-}. The concentration of FL that was removed during incubation was then

determined by measuring the absorbance at 491 nm in UV-Vis spectroscopy, using an

extinction coefficient of 0.238 L mg^{-1} cm^{-1}. The extinction coefficient is in mg of FL^{2-}

and does not include the mass of the sodium ions. Only the mass of the adsorbed species

is included in the adsorption results below. To determine the adsorption capacity, 200 μL

of 1350 ppm CNR (270 μg) was incubated for 30 minutes in dilute NaFL solutions.

Solutions of NaFL were prepared such that the initial concentrations of FL ranged from

0.104 to 3.86 ppm (Table 1). For UV-Vis analysis, a 2.000 mL aliquot was taken for

each sample, and 30 μL of 171.8 mM NaOH was added to the solution before measuring

the absorbance at 491 nm.

Table 1: Adsorption capacity of CNR. C_i is the initial concentration of FL in each sample, A_{491} is the absorbance at 491 nm, C_e is the equilibrium concentration of FL, and q_e is the adsorption capacity of CNR.

Sample	C_i (mg/L)	Equilibrium A_{491}	C_e (mg/L)	q_e (mg FL^{2-} / g CNR)
1	3.86	0.4929	2.07	25.6
2	3.44	0.4073	1.71	24.7
3	3.02	0.3019	1.27	25.1
4	2.61	0.2233	0.938	23.8
5	2.19	0.1298	0.546	23.5
6	1.772	0.07031	0.295	20.99
7	1.355	0.03789	0.159	16.83
8	0.938	0.01765	0.0741	11.91
9	0.521	0.002159	0.0091	6.69
10	0.104	0.004534	0.0191	0.37

2.5 CNR thin-film membrane functionality

Membrane flux experiments were conducted on HPH TONC and CNR. For these experiments, CNR sample material was deposited onto 47 mm diameter, 0.1 μm pore size MCE filters such that the areal density was 1.345 mg cm^{-2} and water flux was measured in L m^{-2} h^{-1} bar^{-1}. Water flux measurements were obtained by passing water under a known positive pressure of nitrogen gas through a circular membrane with known diameter. The volume, V in liters that permeated the membrane was measured as a function of time, and Water Flux, WF was calculated by $WF = \frac{V}{AtP}$ where A is the area of the membrane in squared meters, t is the time in seconds and P is the pressure in bar. Breakthrough curve data was collected by passing 3.965 ppm NaFL through the film, and membrane water flux data was taken before and after adsorbtion of NaFL. Membrane regeneratability was also tested by passing 600 μL of 190 mg/L CNR (114 μg) through a 25 mm diameter 0.2 μm pore size MCE film. NaFL was then pushed through the film using a 10 mL syringe, and the concentration of NaFL was measured before and after

adsorption. Following adsorption, 4 M brine (approximately 20 mL) was then pushed

through the membrane to desorb the NaFL until the concentration of desorbed analyte

was below the detection limit in UV-Vis of 30 ppb. DI water (approximately 60 mL) was

then pushed through the membrane to remove the sodium and chloride ions until the

conductivity measured by a Pharmacia Biotech conductivity flow cell monitor was 0 μS

cm^{-1}. Subsequent cycles were then performed by pushing NaFL through the membrane,

followed by brine and water until 40 cycles had been reached.

CHAPTER 3: RESULTS AND DISCUSSION

3.1 TONC characterization

Carboxylate content of TONC was determined by conductometric titration.

During the titration, conductivity measurements were collected in $\mu S\ cm^{-1}$, and the data

was plotted as a function of the volume of NaOH added. The linear regression of each

line was plotted on the graph and the volume of NaOH required to deprotonate the
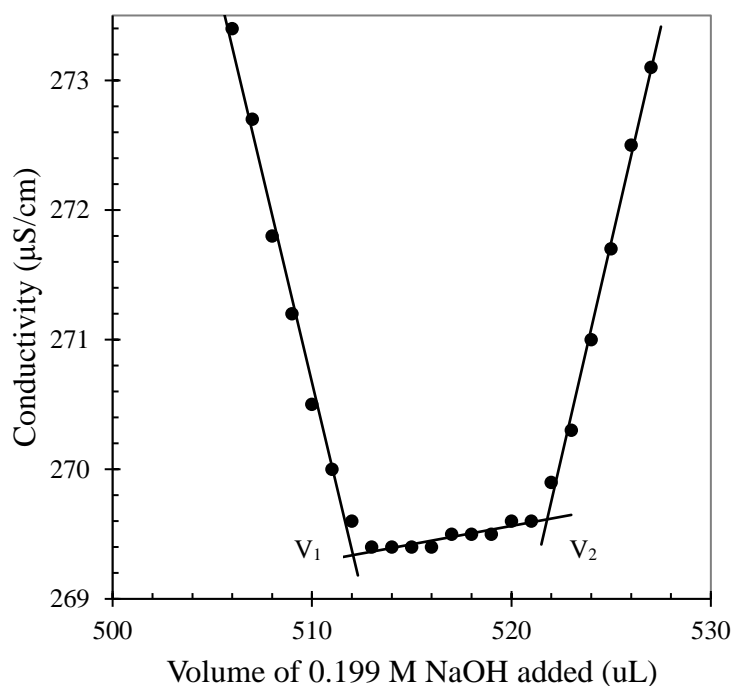
Figure 12: Conductometric titration of TONC. 10.000 mL 96 mg/L TONC titrated with 0.1893 M NaOH. 8.000 μL of NaOH was required to neutralize the weak acid carboxylated groups. Carboxyl content = 1.6 mmol g^{-1}.

carboxyl groups of TONC was determined by subtracting the volume at the 1st

intersection, V_1 from the volume at the 2nd intersection, V_2. As shown in figure 12,

titration of 10.00 mL of 96 mg L^{-1} TONC (0.96 mg, 5.3 μmol) required 8 μL of 0.1893 M

NaOH (1.514 μmol) to completely neutralize the C-6 carboxylate groups. This result

indicates that 28% of all C-6 hydroxyl groups were carboxylated during the oxidation reaction, giving a carboxylate content of 1.6 mmol g^{-1}. Dynamic light scattering (DLS) was used to confirm debundling of the cellulose nanofibrils. Pristine commercial cellulose was dispersed in water and sonicated at 45 W cm^{-2} for 3 hours. The dispersion was then centrifuged at 3000 g at 20 °C for 20 minutes. The transparent solution of cellulose fibrils was then diluted in 0.1 mM potassium chloride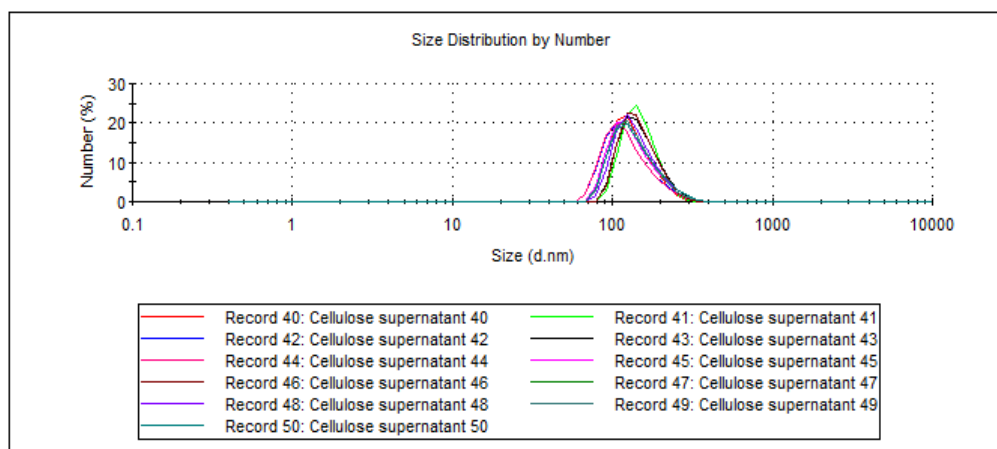 solution for DLS analysis. Figure 13a and 13b show the particle size as hydrodynamic diameter for cellulose and TONC, respectively. The hydrodynamic diameter of the cellulose fibrils decreased from 142.1 nm to 30.08 nm after oxidation, indicating successful debundling of the cellulose nanofibrils. The zeta potential of cellulose was also measured before and after oxidation. As shown in figure 14, the zeta potential was determined to be -0.0999 mV and -27.7 mV for cellulose and TONC, respectively. The negative surface charge of the TONC product is indicative of successful oxidation when compared to the relatively neutral surface charge of the pristine cellulose.

a)

		Size (d.nm):	% Number	Width (d.nm):
Z-Average (d.nm): 243.2	Peak 1:	142.1	100.0	49.32
Pdl: 0.389	Peak 2:	0.000	0.0	0.000
Intercept: 0.932	Peak 3:	0.000	0.0	0.000

Result quality : Refer to quality report

Size Distribution by Number

Record 40: Cellulose supernatant 40
Record 41: Cellulose supernatant 41
Record 42: Cellulose supernatant 42
Record 43: Cellulose supernatant 43
Record 44: Cellulose supernatant 44
Record 45: Cellulose supernatant 45
Record 46: Cellulose supernatant 46
Record 47: Cellulose supernatant 47
Record 48: Cellulose supernatant 48
Record 49: Cellulose supernatant 49
Record 50: Cellulose supernatant 50

b)

		Size (d.nm):	% Number	Width (d.nm):
Z-Average (d.nm): 311.1	Peak 1:	222.6	0.1	64.49
Pdl: 0.494	Peak 2:	30.08	99.9	5.855
Intercept: 0.955	Peak 3:	0.000	0.0	0.000

Result quality : Refer to quality report

Size Distribution by Number

Record 45: Celluouronic Acid (96 mg/L) 31
Record 46: Celluouronic Acid (96 mg/L) 32
Record 47: Celluouronic Acid (96 mg/L) 33
Record 48: Celluouronic Acid (96 mg/L) 34
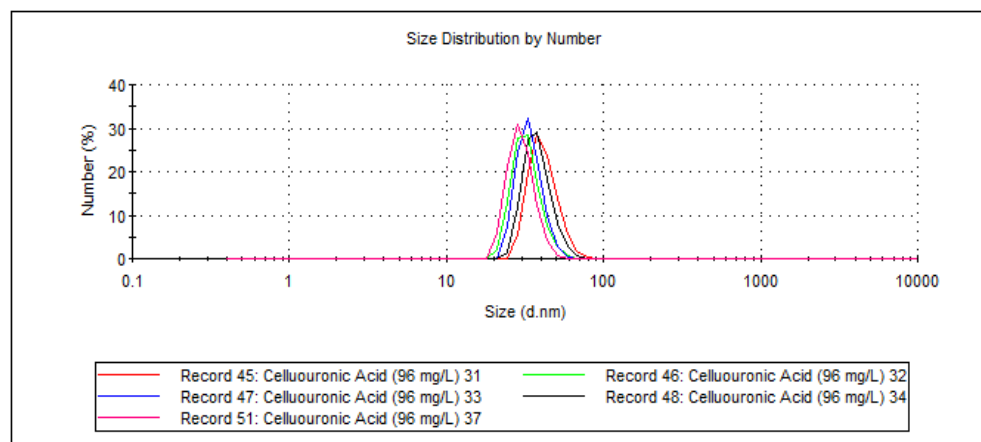Record 51: Celluouronic Acid (96 mg/L) 37

Figure 13: DLS size distribution for cellulose (a) and TONC (b). Hydrodynamic diameter decreases from 142.1 nm in cellulose to 30.08 nm in TONC, indicating successful debundling of the cellulose nanofibrils.

a)

		Mean (mV)	Area (%)	Width (mV)
Zeta Potential (mV): -0.0999	Peak 1:	-0.0999	100.0	2.58
Zeta Deviation (mV): 2.58	Peak 2:	0.00	0.0	0.00
Conductivity (mS/cm): 0.0292	Peak 3:	0.00	0.0	0.00

Result quality : See result quality report

b)
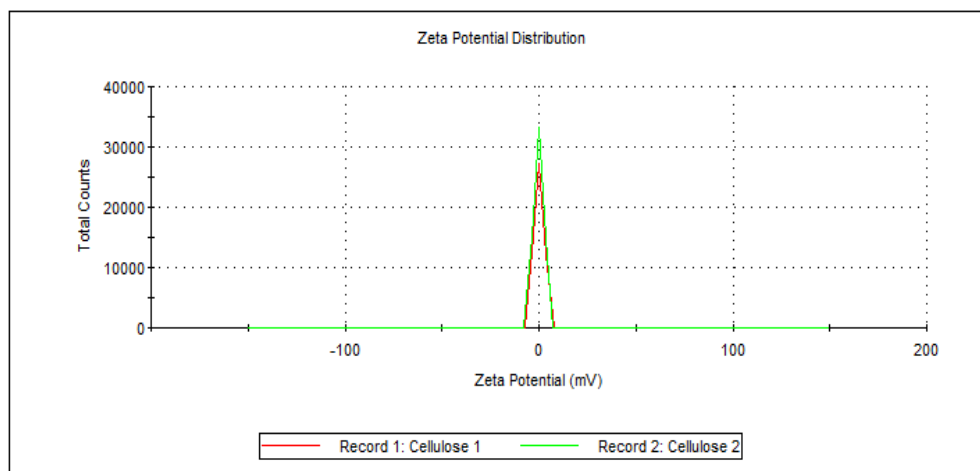
		Mean (mV)	Area (%)	Width (mV)
Zeta Potential (mV): -27.7	Peak 1:	-27.7	100.0	7.76
Zeta Deviation (mV): 7.76	Peak 2:	0.00	0.0	0.00
Conductivity (mS/cm): 0.0123	Peak 3:	0.00	0.0	0.00

Result quality : Good
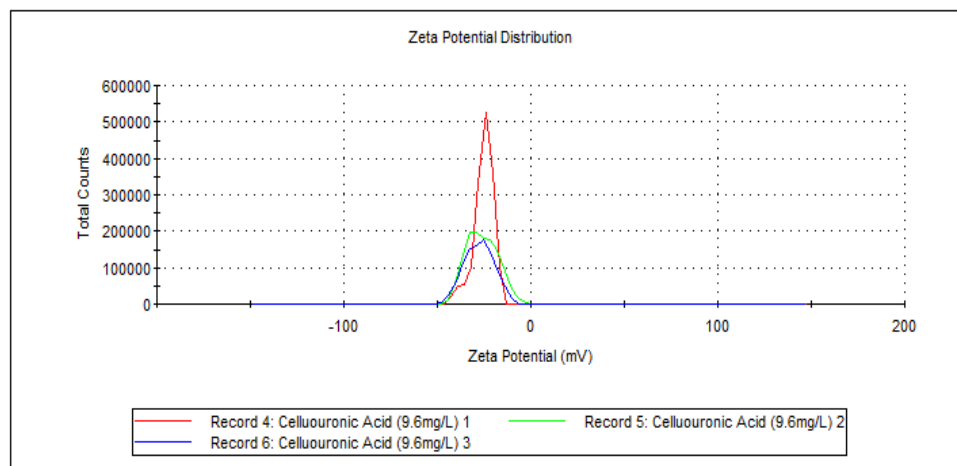
Figure 14: Zeta potential for cellulose (a) and TONC (b). Surface charge of cellulose changed from relatively neutral to negative after TEMPO-mediated C-6 carboxylation. This result is evidence of negative surface charge due to the introduction of carboxyl groups on the cellulose surface.

a)

b)

Figure 15: FTIR of cellulose (a) and CNR(b). New peaks at 1644 cm^{-1} and 798 cm^{-1} indicate C=O stretching from styrene rings and C-Br stretching from HEBIB.

3.2 CNR characterization

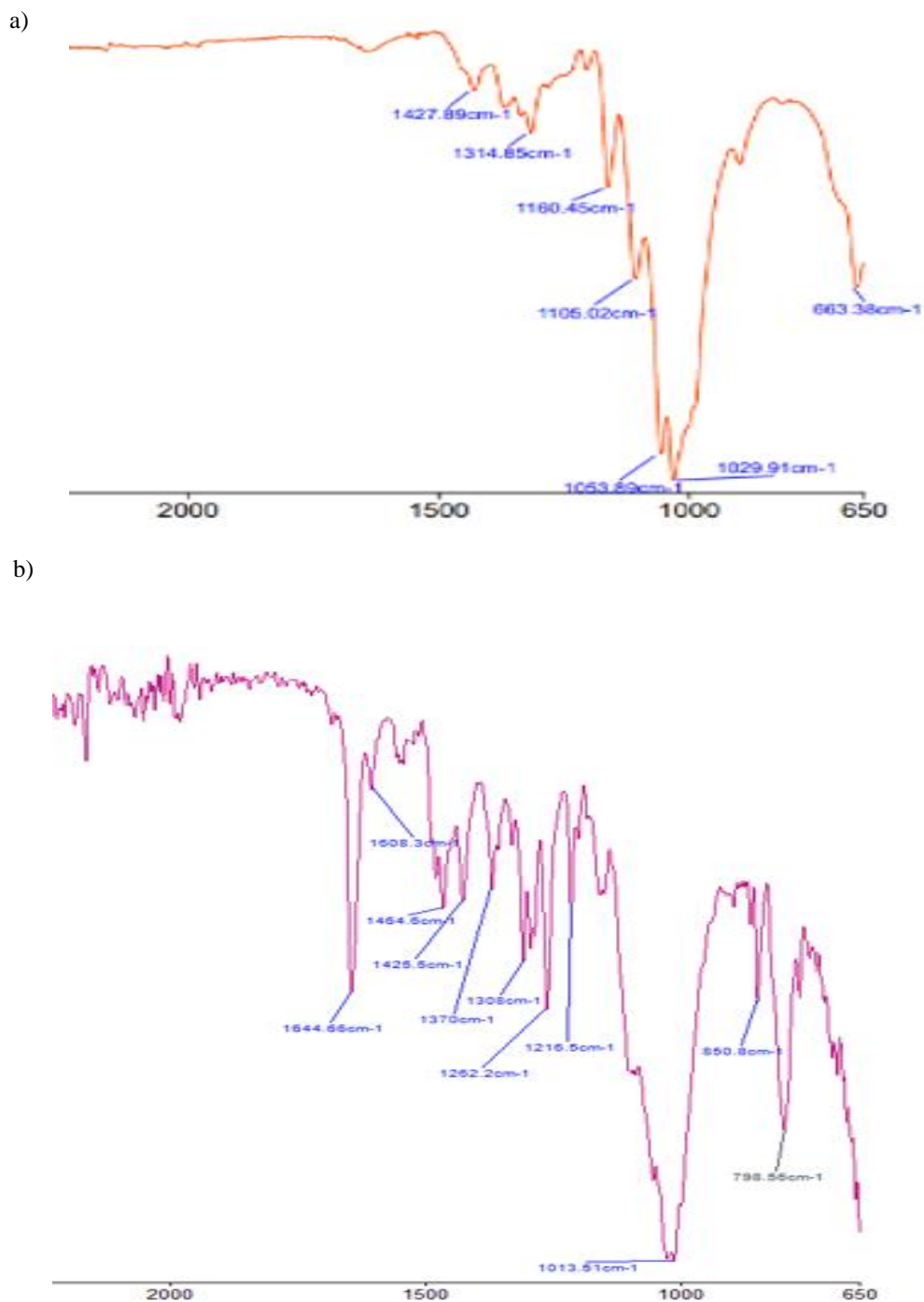CNR synthesis was monitored by Fourier transform infrared spectroscopy (FTIR) and DLS. Pristine cellulose showed clear peaks at 3334 cm^{-1}, 2893 cm^{-1} and 1053 cm^{-1}, indicating O-H, C-H and C-O stretching (figure 15). The peak at 1053 cm^{-1} is indicative of the β 1,4-glycosidic linkages. After the coupling of the polyelectrolyte to TONC, FTIR showed new peaks at 1664 cm^{-1} and 798 cm^{-1}. This is evidence of C=C stretching from the styrene rings in poly(vbTMAC) and C-Br stretching from the HEBIB initiator.

The hydrodynamic diameter and zeta potential were measured for CNR. Results are shown in figure 16. An increased size from 30.08 nm to 207.9 nm suggests that TONC was successfully functionalized with poly(vbTMAC). Additionally, a positive zeta potential of +17.3 mV is consistent with the grafting of poly(vbTMAC) and its quaternary ammonium cations to the cellulose backbone.

a)

		Size (d.nm):	% Number	Width (d.nm):
Z-Average (d.nm): 882.2	Peak 1:	207.9	100.0	33.74
PdI: 0.832	Peak 2:	0.000	0.0	0.000
Intercept: 0.654	Peak 3:	0.000	0.0	0.000

Result quality : Refer to quality report

b)
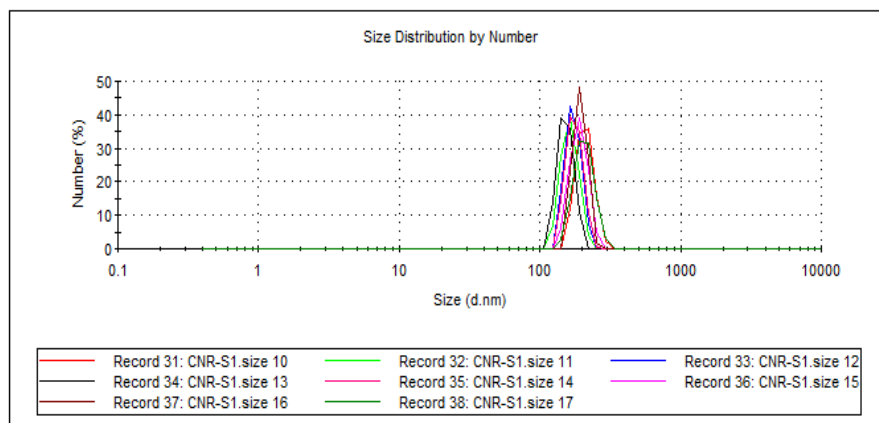
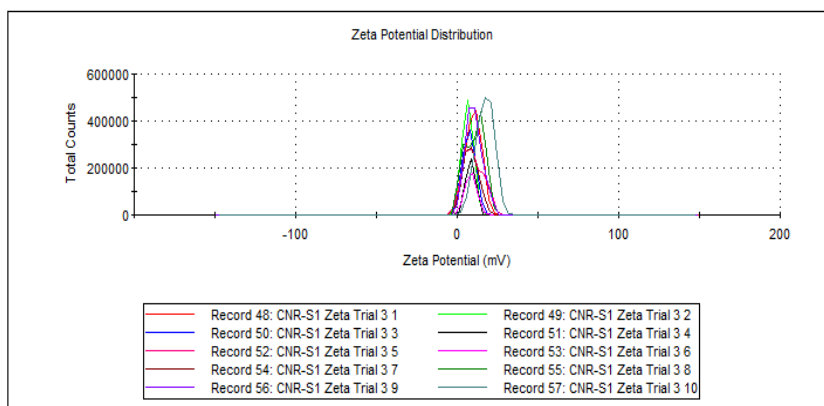|		Mean (mV)	Area (%)	Width (mV)
Zeta Potential (mV): 17.3	Peak 1:	17.3	100.0	5.42
Zeta Deviation (mV): 5.42	Peak 2:	0.00	0.0	0.00
Conductivity (mS/cm): 0.100	Peak 3:	0.00	0.0	0.00

Result quality : Good

Figure 16: Size (a) and zeta potential (b) of CNR. Hydrodynamic diameter of cellulose increased after functionalization of poly(vbTMAC). Zeta potential is positive (+17.3 mV) due to the introduction of positively charged polyelectrolyte strands.

CNR PF was measured using conductometric titration. 3.000 mL (0.288 mg, 1.60

μmol) of CNR was added to 100 mL of water along with 100.0 μL of 0.1000 N HCl,

bringing the pH to 2.93. The mixture was then titrated with 17.18 mM NaOH. The

volume of NaOH needed to reach complete neutralization of both HCl and the

carboxylate groups of TONC were determined by using linear regression data analysis as

described above. The intersection of the line with zero slope with the lines with negative

and positive slopes correspond with the volumes at which neutralization was completed

for HCl and TONC, respectively. Complete neutralization of HCl and of the C-6

carboxylate groups of CNR required 19.45 mL and 13.00 μL of 17.18 mM NaOH

(0.2233 μmol), respectively (figure 17). This result indicates a carboxylate content of
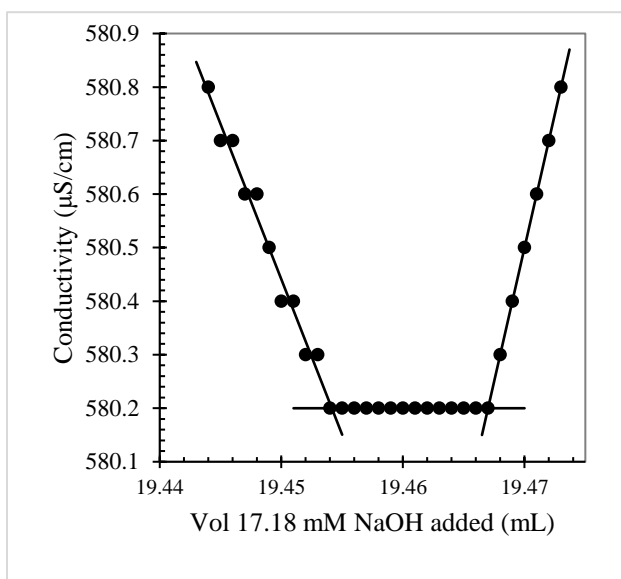
0.775 mmol/g and a PF of 50.9 %.

Figure 17. Conductometric titration of CNR
using 17.18 mM NaOH. Neutralization of
carboxylated C-6 groups in 288 μg of CNR
required 0.2233 μmol NaOH.

The PF of TONC was measured as a function of the mole ratio of poly (vbTMAC) to TONC carboxyl groups during esterification. TONC esterification was performed for 72h each using mole ratios of 0.1, 0.5, 1, and 2. Conductometric titration data for each product was used to calculate PF as shown in figure 18. The PF approached 60.7% as the mole ratio of poly (vbTMAC) polymer strands to TONC carboxyl groups was increased from 0.1 to 2. From these data it is evident that increasing the mole ratio of poly (vbTMAC) leads to an increase in the percent functionalization of TONC carboxyl groups. In future studies of these CNR materials, mole ratios higher than 2 should be conducted to confirm that percent functionalization continues to level off.

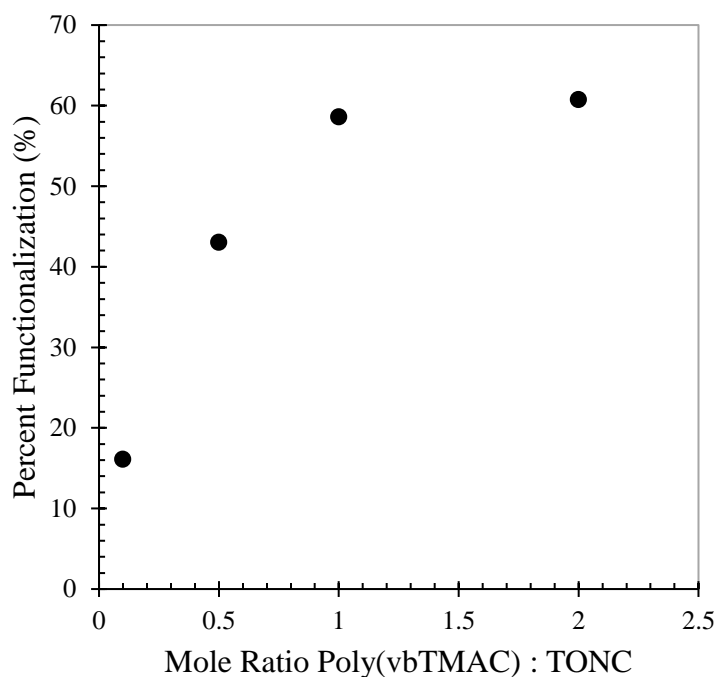Figure 18: Percent functionalization as a function of the mole ratio of poly(vbTMAC) to TONC carboxyl groups during esterification. Maximum percent functionalization is achieved at a 2:1 mole ratio.
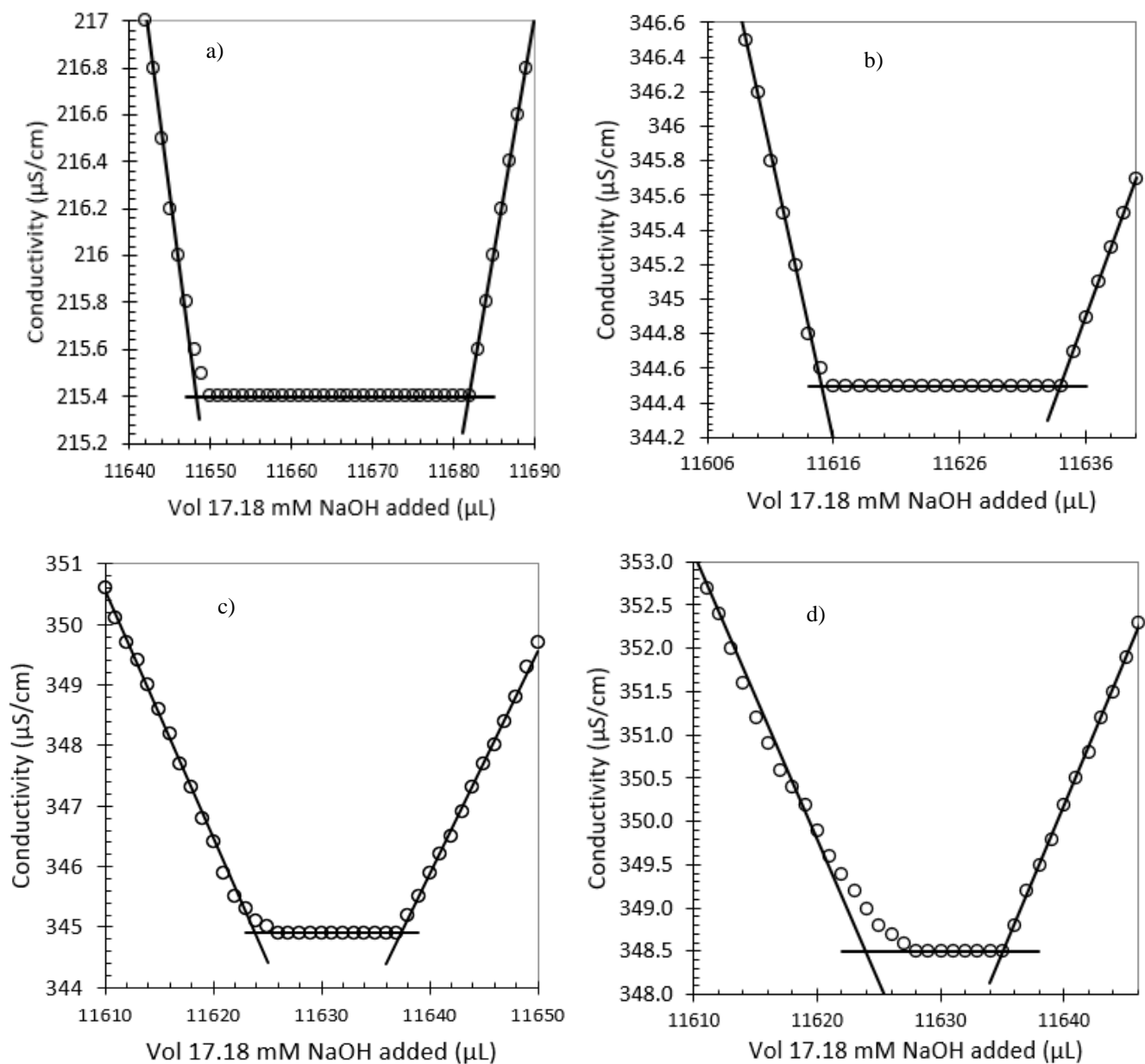
Figure 19: Conductometric titration of CNR synthesized using mole ratios of 1:10 (a), 1:2 (b), 1:1 (c), and 2:1 (d) poly(vbTMAC) to sonicated, pH controlled TONC. Maximum percent functionalization was achieved using a 2:1 mole ratio.

Figure 20a and 20b show the hydrodynamic diameter in nm and positive zeta potential in mV, respectively, as a function of mole ratio. A maximum hydrodynamic diameter of 198.2 nm and surface charge of +15.9 mV were both achieved by performing the esterification reaction using a 2:1 mole ratio of poly(vbTMAC) to TONC carboxyl groups. The increase in size and positive surface charge of the nanocellulose can both be attributed to the introduction of polyelectrolyte strands with cationic active binding sites. These data are consistent with results from conductometric titration experiments. Based on these results, a 2:1 mole ratio was used for all future synthesis of CNR.
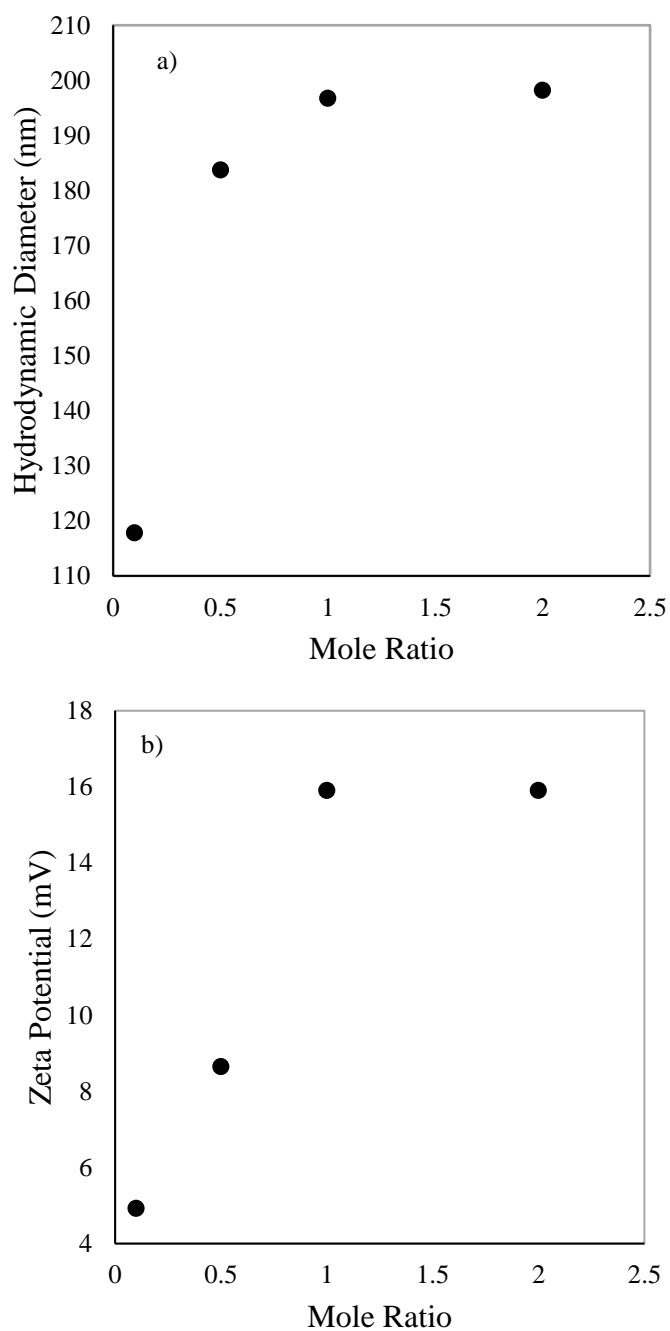
Figure 20: Hydrodynamic diameter (a) and positive zeta potential (b) as a function of the mole ratio of poly(vbTMAC) to TONC carboxyl groups during acid-catalyzed esterification. Maximum size of 198.2 nm and surface charge of +15.9 mV is achieved at a 2:1 mole ratio.

3.3 Optimization of TONC synthesis

The TONC esterification reaction was performed six times with reaction time intervals ranging from 1 h to 24 h using a 2:1 mole ratio of poly(vbTMAC) to TONC carboxyl groups. Figure 21 shows the PF as a function of esterification reaction time. Maximum PF of 61.1 % was achieved after 17 h of reflux. DLS size and surface charge measurements (figure 22) yielded consistent data with a maximum hydrodynamic diameter of 190.2 nm and zeta potential of +15.5 mV both occurring at a reaction time of 17 h.

Figure 21: Percent functionalization of TONC as
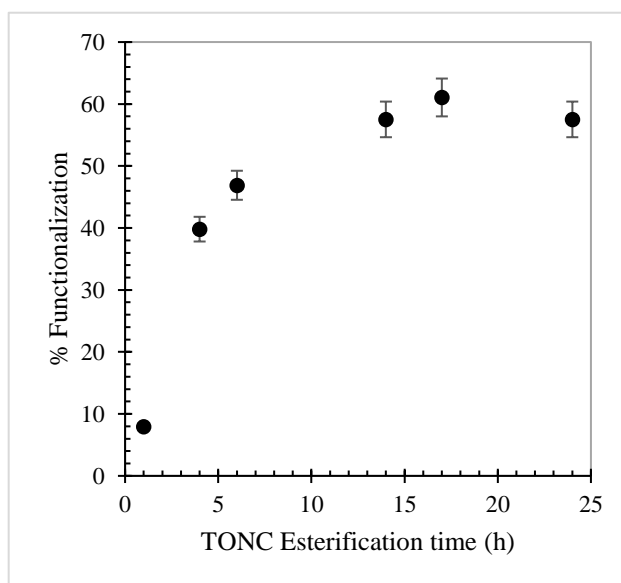a function of esterification reaction time.
Maximum percent functionalization of 61.1 %
was achieved by allowing 17 h of reflux.
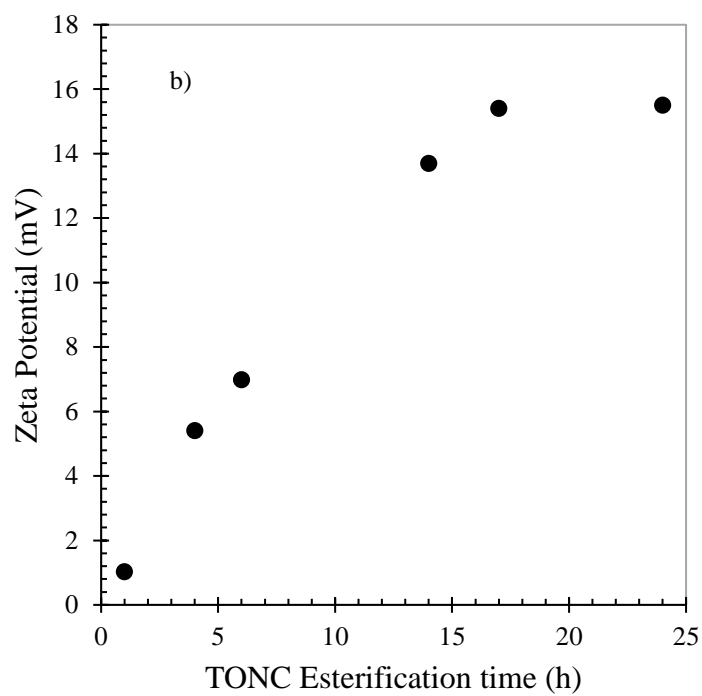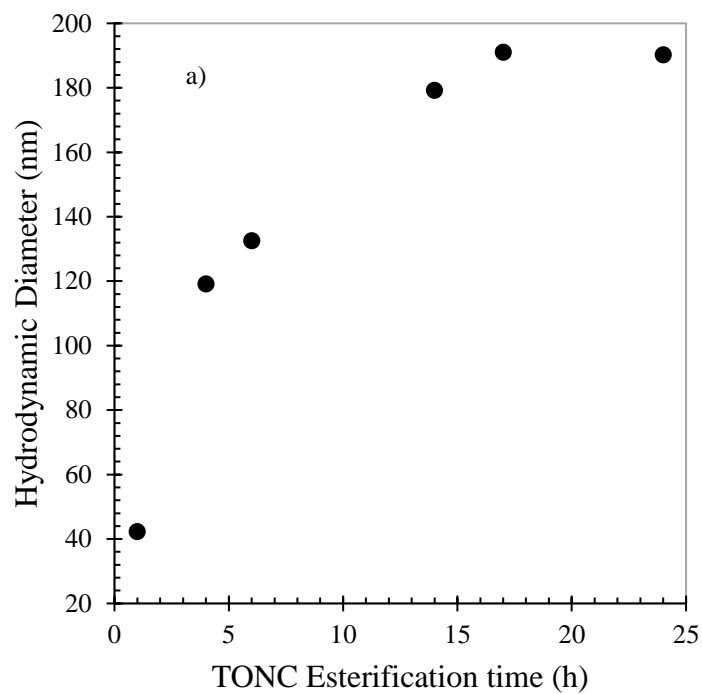
Figure 22: Hydrodynamic diameter (a) and zeta potential (b) as a function of esterification reaction time. Maximum size of 190.2 nm and zeta potential of +15.5 mV achieved at 17 h reaction time.

3.4 CNR adsorbent thin-film membrane functionality

The adsorption capacity of CNR was determined using a NaFL surrogate adsorbate. The initial and equilibrium concentration of NaFL for each of the seven samples can be found in table S1. For each sample, 200 μL (37.2 μg) of 186 mg/L CNR was added to NaFL such that the total volume was 2.000 mL. Each sample was allowed to incubate for 30 minutes. The equilibrium concentration of NaFL was calculated by

Model	Langmuir (User)		
Equation	qm*(Ks*Ce/(1+Ks*Ce))		
Reduced Chi-Sqr	4.69326		
Adj. R-Squar	0.93988		
		Value	Standard Err
qe	qm	26.7929	1.33008
qe	Ks	10.4727	2.66806

Model	Freundlich (User)		
Equation	Kf*Ce^(1/nf)		
Reduced Chi-Sqr	13.69625		
Adj. R-Square	0.82455		
		Value	Standard Error
qe	Kf	23.33738	1.4208
qe	nf	3.85681	0.78912

Figure 23: Adsorption capacity of CNR using surrogate NaFL. Q_{max} for CNR was 26.7 ± 1 mg NaFL per gram.

measuring the absorbance at 491 nm. For NaFL, $\varepsilon_{491} = 0.260$ mg^{-1} L cm^{-1} and the limit of

detection is 30 ppm. Adsorption capacity qe was calculated as mg of adsorbed NaFL per

gram of CNR. Figure 23 shows the equilibrium loading capacity (q_e) of CNR as a
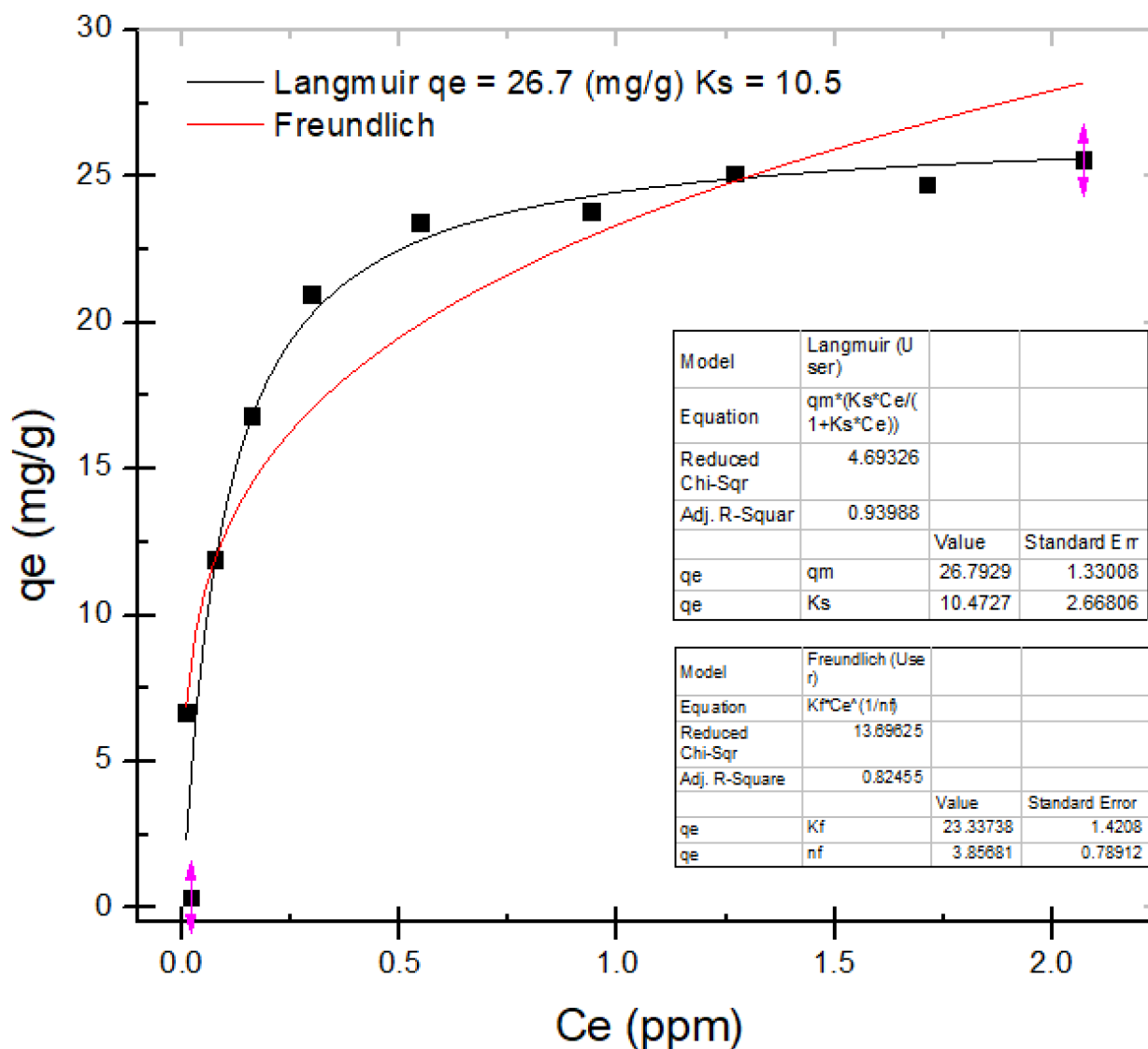
function of equilibrium concentration (C_e). The Langmuir and the Freundlich models

were fit to the loading capacity data. The Langmuir model – a modified form of the BET

adsorption model, is a theoretical construct that assumes the adsorbate binds to the

adsorbent with mono-layer surface coverage only. The Freundlich model is an empirical,

phenomenological model that does not have this mono-layer restriction. The Langmuir

model was a better fit to the data in this case, with a reduced Chi-Square value of 4.69

and an R^2 value of 0.940. This analysis indicates that the maximum adsorption capacity,

q_{max} of CNR is 26.7 ± 1 mg NaFL per gram of CNR and that the equilibrium constant of

adsorption, $K_s = 10.5 \pm 3$, indicating thermodynamically favorable adsorption.

The performance of CNR as thin-film adsorbent membranes was tested by measuring membrane water flux and breakthrough curve data. The membrane water flux of HPH TONC and CNR was measured to be 281 and 783 L m^{-2} h^{-1} bar^{-1}, when tested using 0.1 μm pore size, 47 mm MCE films with areal densities of 1.412 and 1.345 mg cm^{-2}, respectively. Breakthrough curve data for CNR adsorbing NaFL is shown in figure 24. The water flux of CNR after adsorbing NaFL was measured to be 707 L m^{-2} h^{-1} bar^{-1}.
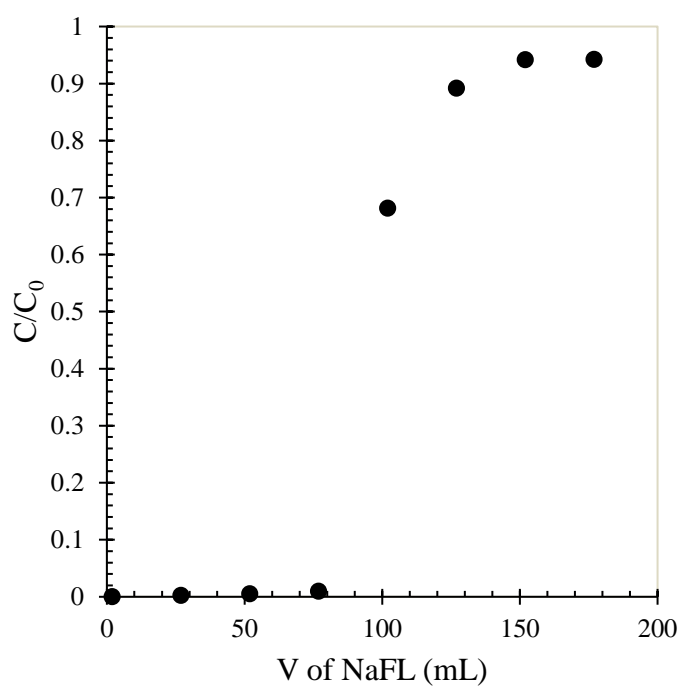
Figure 24: Breakthrough curve of CNR adsorbing NaFL. Concentration of NaFL = 3.965 ppm and areal density of CNR membrane is 1.000 mg cm^{-2}.

3.5 CNR membrane regeneration

CNR thin film regenerability was tested by first pushing 114 µg CNR through a 0.2 µm MCE film to make the nanoresin membrane. Then, 5.000 mL of 1.75 ppm NaFL (8.75 µg) was pushed through the membrane and the absorbance at 491 nm was measured before and after adsorption using UV-Vis spectroscopy. The measured absorbance of 0.290 was then used to calculate the equilibrium concentration of 1.22 ppm using the Beer-Lambert law. Using the initial volume of NaFL, the mass of analyte in the effluent was 6.10 µg, meaning that 2.65 µg had been adsorbed by 0.114 mg CNR, giving a loading capacity, q_e = 23.2 mg NaFL per gram of CNR. The membrane was then regenerated with approximately 20 mL of 4M NaCl and the concentration of NaFL in the brined effluent was calculated to be less than the detection limit of 30 ppb. DI water was passed through the membrane until the conductivity reached 0 µS cm^{-1} and the process was repeated for a total of 40 cycles. Figure 25 shows the loading capacity, q_e as a function of cycle number. A linear regression was used to model the efficiency loss per cycle of adsorption/regeneration. As shown in figure 24, the loading capacity of the CNR membrane decreased by -0.01 ± 0.01 mg NaFL per gram CNR per cycle. These data suggest that, in addition to functioning with high adsorptive capacities and high-water flux, these ion-exchange CNRs are regeneratable and reusable materials when used as water purification membranes.
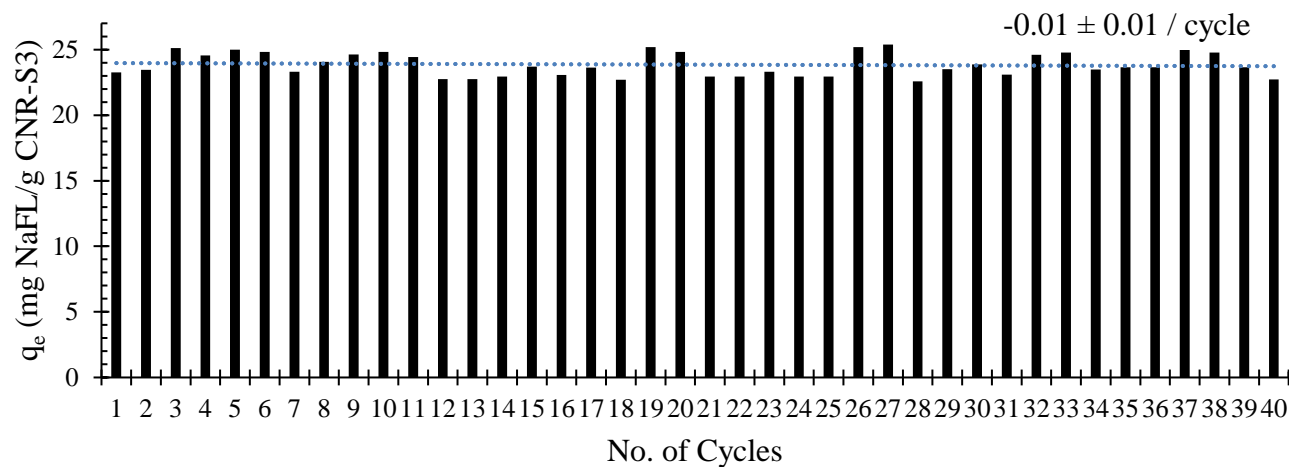
Figure 25: Regeneratability of CNR membrane. Loading capacity, q_e shown as a function of cycle number. Membrane functionality as a water purification thin-film membrane decreased by 0.01 ± 0.01 mg NaFL per gram of CNR after 40

CHAPTER 4: CONCLUSIONS

Cellulose-based ion-exchange nanoresins have been synthesized in an aqueous medium. Successful synthesis was confirmed by FTIR, conductometric titration, zeta potential measurements and DLS. Peaks in the IR spectrum of CNR at 1644 cm^{-1} and 798 cm^{-1} indicate C=O stretching from styrene rings and C-Br stretching from HEBIB, respectively. Conductometric titration revealed a carboxyl content of 1.6 mmol/g in TONC, and a percent functionalization of 60.7% in CNR. The surface charge of cellulose, TONC, and CNR was neutral, negative, and positive, indicating the anionic carboxylate groups on the TONC surface and the cationic quaternary ammonium binding sites on the surface of CNR. The size of the dispersed particles in commercial cellulose decreased from 142.1 nm to 30.08 nm after sonication at 72 W cm^{-2} for 2 hours. After functionalization with poly (vbTMAC), the size of the cellulose graft copolymer increased to 207.9 nm.

These CNR materials consist of oxidized cellulose coupled to cationic polyelectrolyte strands. Cellulose was debundled by sonication and oxidized at the C-6 position of the D-glucose monomer via the TEMPO radical. Poly(vbTMAC) and CNR synthesis was achieved via ARGET-ATRP and acid-catalyzed Fischer-Speier esterification, respectively. In our previous work, we have shown that similar materials, such as poly (vbTMAC) covalently coupled to single-walled carbon nanotubes (SWCNT) and to fluorographite (FGi) nanoplatelets, can be used to remove several important anionic contaminants from drinking water.[41, 42] Cellulose nanoresins will provide a more cost-effective alternative to previously published anion-exchange water purification materials while maintaining high efficiency as regenerable adsorbent membranes.

Our CNR materials exhibit high water flux of >700 L m^{-2} h^{-1} bar^{-1} and high

loading capacities of >20 mg g^{-1} when tested using NaFL surrogate adsorbate. Water

flux measurements for these CNR materials are similar to values that we have measured

for functionalized SWCNTs, which were found to have a water flux of 692 L m^{-2} h^{-1} bar^{-1}

for membranes with similar areal densities.[42] CNR membranes also outperformed FGi

membranes in loading capacity of surrogate contaminant NaFL, with values as high as

23.3 mg NaFL / g CNR compared to 17.9 mg NaFL / g FGi in functionalized

fluorographite.[41]

These CNR materials exhibit fast adsorption kinetics, with equilibrium loading

being achieved in a matter of seconds. CNR membranes are regenerable, with a decrease

of only 0.01 ± 0.01 mg NaFL adsorbed per gram of CNR over the course of 40 cycles. In

the current point-of-use (POU) water filtration sector, commercialized filters such as

activated carbon, reverse osmosis, and distillation units are not advertised for their ability

to be regenerated and reused. Instead, most homeowners simply throw away their water

filters after using them for a suggested amount of time. As a student in the National

Science Foundation's Ventureprise Launch NSF I-Corps program through the University

of North Carolina at Charlotte, I was tasked with conducting a minimum of thirty

interviews with homeowners and business owners who would potentially use a POU

water filter. According to most interviews with homeowners and business owners, many

people would be willing to pay more initially for a water filter that is regeneratable and

reusable for two main reasons – not only will this solution save customers money in the

long term, but it will also reduce plastic waste that is made from throwing away old water

filters. In addition to the Ventureprise experience, I was also able to attend the Water

Environment Federation's Technical Exhibition and Conference (WEFTEC), where I was able to conduct interviews with industry experts. From the interviews at WEFTEC, I learned that several companies in the water sector are focusing on designing new technologies that can be used to retrofit existing or outdated ones. Considering our nanoscale water purification technologies, we learned that it would be important for us from a marketing perspective to build our membrane filters in a way that will be adaptable to POU water filters of any existing brand. We believe that, while this may require additional experience from an engineering perspective, having the ability to avoid reinventing the wheel will pay off in the long run.

Currently, the United States Environmental Protection Agency is focused on the removal of several classes of water contaminants, including disinfection byproducts, pharmaceuticals, pesticides, heavy metals, and per-and polyfluoro alkyl substances (PFAS). Many of these harmful chemicals listed above have maximum contaminant levels of 1-100 ppb, while PFAS chemicals have health advisory limits of 70 ppt. PFAS chemicals such as perfluorooctanoic acid (PFOA) and perfluorooctane sulfonate (PFOS) have been linked to breast and ovarian cancer, endometriosis, thyroid disruption, immunosuppression, diminished childhood antibody responses to vaccinations, and adverse placental and birth outcomes including low infant birth weights.[43, 44] Recent studies have found that, compared with the general public, anglers consuming wild fish have higher exposure levels to PFAS.[45] In addition, areas in proximity to military bases, airports, firefighter training facilities and industrial sites are at higher risk of elevated PFAS contamination.[46, 47] To address the problem of chemical drinking water contamination, we have previously developed novel nanoscale technologies of

functionalized SWCNTs and FGi for use as ion-exchange membranes, which were capable of removing >99% of PFOA to below 100 ppt.[41] What is reported in this thesis is the covalent grafting of a polyelectrolyte to oxidized cellulose. We are confident that, like our previously synthesized materials, CNR will also be capable of removing PFAS from drinking water by ion-exchange. These nanoresins will be engineered to retrofit existing POU water filtration technologies, and will be regeneratable and reusable. With our cellulose nanoresins, we hope to provide an affordable yet effective, efficient, and safe solution to the problem of chemical drinking water contamination.

APPENDIX: SUPPLEMENTAL INFORMATION & DATA

S1: INTRODUCTION

S1.1 Isothermal Titration Calorimetry Background

Isothermal titration calorimetry is an established method to measure binding interactions of small molecules (ligands) to larger macromolecules like proteins and polymers. ITC is used to determine the binding association constant (K_a), binding site stoichiometry (n), enthalpy of binding (ΔH_b), entropy of binding (ΔS_b), and Gibbs free energy of binding (ΔG_b) of various protein-ligand interactions.[48, 49] The advantage of this method is that all thermodynamic variables can be determined from a single ITC experiment. The ITC instrument operates by maintaining a constant temperature in the sample cell versus the reference cell. If a reaction is exothermic, the system removes energy from the sample cell and if the reaction is endothermic then it adds heat energy to the sample to maintain the isothermal status. The amount of heat energy removed or added by the ITC is equal and opposite to that lost or gained during the titration reaction. The sample cell is typically loaded with a macromolecule, such as DNA, polymer, or protein. A titration syringe is used to inject a small volume of ligand solution into the sample cell at fixed time intervals. A thermoelectric cooler is used to maintain constant temperature during the reaction at each injection. A reference cell is used to constantly compare the temperature of the sample cell to a point of reference while the reaction occurs.[50]

Over the course of a titration reaction, a predetermined volume of titrant is injected into the sample cell. The titration burette is designed to simultaneously stir the reaction. Typically, a stir rate of 200-300 RPM is used for the Low Volume (190 µL)

NanoITC. Data is collected as power, or heat rate, measured in $\frac{\mu cal}{s}$ or $\frac{\mu J}{s}$ (μW) vs. time, measured in seconds. The thermogram peaks are then integrated, after baseline correction, to yield the measured heat energy released or absorbed during the reaction. As the experiment proceeds, peak power of the thermograms falls off as a sigmoidal curve, and analysis of the shape and position of the curve as a function of mole ratio leads to the acquisition of the data listed above. A plot of the integrated area of the thermograms vs. the mole ratio can be modeled based on the number of moles of sample solution and the number of moles of injectant added. The inflection point of this plot gives the stoichiometry, (n) of the reaction, and the slope of the curve at the midpoint gives the association constant, (K_a). An example of a typical ITC graph and subsequent mole ratio plot is shown in Figure 1. The enthalpy of the binding interaction can be directly measured by integrating the area of the 2nd thermogram of the graph and dividing by the number of moles of injectant. The 2nd thermogram is analyzed for the measurement of molar enthalpy because the 1st thermogram typically shows less heat than expected due to the diffusion of the tip of the needle, small air bubbles at the needle or tip, or differences in positioning of the burette drive.[50] Once ΔH_b and K_a are determined, ΔG_b and ΔS_b can be calculated by the equation: $\Delta G = -RT\ln K_a = \Delta H - T\Delta S$, where R is the ideal gas constant and T is the Kelvin temperature.
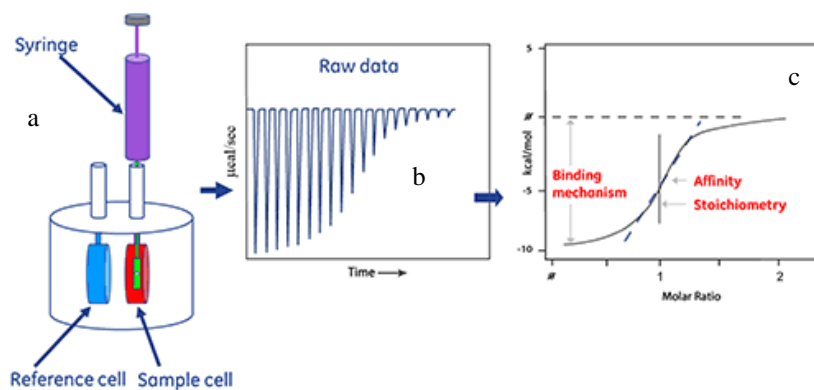
Figure S1: Example ITC data. Physical apparatus (a), raw baseline data (b), and (c) injection plot

S1.2: Recent Applications of ITC

Isothermal titration calorimetry has been used to characterize interactions of a large variety of proteins with ligands functionalized with nanoparticles (NPs).[51] For example, Rotello *et al.* found in 2007 that the binding of several amino acids functionalized with Au NPs to R-chymotrypsin (ChT) was driven enthalpically, while the binding to histone, and cytochrome c(CytC) was driven entropically, with CytC having two separate binding events.[52] Wang *et al.* studied the interaction of proteins with carbohydrates functionalized with Au NPs.[53] The group specifically worked with mannose and galactose and studied the binding interaction of Concanavalin A (Con A) and Peanut Agglutinin (PNA). Wang's group found in 2012 that the adsorption of Con A on mannose-coated NPs was enthalpically driven and that the stoichiometry depended on the ligand density of the NP. Wang reported no detection of adsorption of PNA on mannose-coated NPs and of Con A on galactose-coated NPs. Characterization of the binding interaction of 15N-labeled ubiquitin onto N-benzoyllysine- and 4-aminohippuric acid-coated Au NPs was reported by Srinivasan in 2014.[54] The study found that

adsorption on N-benzoyllysine was driven entropically and that n ≈ 5. Additionally, adsorption on 4-aminohippuric acid was endothermic at low temperatures but exothermic at high temperatures, and n ≈ 5, K_b ≈ 10^5.

ITC has also been used to characterize the adsorption processes of water purification systems. Peng *et al.* was able to detect heat exchange in the adsorption of heavy metals including lead(II), manganese(II), chromium(III) and cadmium(II) onto polystyrene nanospheres for extraction from collagen solutions.[55] This study reported in part that the ΔG and ΔS values were negative and positive, respectively for each of the tested metals. Drout *et al.* used ITC to characterize adsorption mechanisms in metal-organic frameworks (MOFs) using glyphosate – the active ingredient in the pesticide Roundup.[56] The group proposes MOFs as strong candidates for cost-effective water purification methods, and further asserts that ITC will contribute to the design of such methods.

The removal of molecular contaminants is becoming increasingly difficult for current water treatment facilities.[57] Substances such as per- and polyfluoroalkyl substances (PFAS), disinfection byproduct (DBP) precursors, heavy metals, and other pervasive and persistent contaminants are all substances that have deleterious health effects which must be removed using advanced methods. Ion-exchange membranes for permselective removal of harmful water contaminants have been studied extensively.[58] Isothermal Titration Calorimetry (ITC) is typically used to measure the thermodynamics and kinetics of binding interactions in enzyme catalysis, though little research has been done to measure the effectiveness of ion-exchange polymer resins for water purification.[59] The Poler research group aims to contribute to the already established field of protein-ligand

binding analysis and primarily to establish thermodynamic and kinetic characterization of

novel water purification methods through ITC.

S2: EXPERIMENTAL METHODS

S2.1: Materials

Titrations were performed using the NanoITC Low Volume (190 µL) instrument from TA Instruments. The 50 µL titration syringe from TA Instruments was used for the injection of titrant solutions, while the sample cell was loaded using a Hamilton 500 µL gas tight syringe. A Degassing Station from TA Instruments was used to degas the solvents that were placed in the reference cell. Solutions were made and diluted using 100-1000 µL, 10-100 µL, and 0.1-2.5 µL Eppendorf micropipettes and the corresponding general purpose Redi-Tips from Fisher Scientific. A Denver Instruments M-120 Mass Balance was used along with a Mettler Toledo XS105 to measure the mass of solids used in making solutions, and a National Appliance Company Drying Oven (Model No. 5831) was used to dry solids before massing. Data collection occurred in the ITCRun program from the NanoSeries software package from TA instruments, and data was modelled using the NanoAnalyze program.

S2.2: Water – Water Titration

To assess the performance of the NanoITC instrument, a water – water titration was performed. Distilled, deionized (DD) water was injected into DD water and the work of friction during the injections was observed. Following a 10-minute degassing of the DD water, 50 µL and 300 µL of DD water was loaded into the syringe and sample cell, respectively. Ten injections of 4.99 µL aliquots were injected at 500 s intervals while stirring at 250 RPM at 25 °C. The data was modelled using the Blank (constant) style to observe the average work of friction of the 10 injections.

S2.3 Tris Base – HCl Titration

A tris base - HCl reaction was performed to check and correct the instrument's calibration. The enthalpy of protonation during the reaction was measured and compared to a known value. The HCl was prepared by diluting a 0.1 N HCl stock solution (0.0999N ± 0.00007N) from Brinkmann Certified Titrants (Lot No. 8141-17, CAS No. 7647-01-0) to 1.000 mM by diluting into DD water. The tris base was prepared by diluting a 250 mM stock solution of tris base (CAS No. 77-86-1) to 5.0×10^1 mM by diluting into DD water. A sample of DD water was then degassed for 15 min under vacuum pressure of 635 mmHg and loaded into the reference cell of the NanoITC. The sample cell was then filled with 3.000×10^2 μL of 5.0×10^1 mM tris base and the burette syringe was filled with 50 μL of 1.000 mM HCl. A titration was performed where 10 injections of 4.99 μL were made every 200 s while stirring at 250 RPM at 25 °C. The data was modelled using the enthalpy screening method to observe the accuracy of the enthalpy measurements of the instrument.

S2.4 HCl Standardization

A similar experiment of HCl – base titration was repeated using NaOH in place of tris base for preparation in the sample cell of the NanoITC instrument. The same HCl stock solution from section 2.3 was standardized using an aqueous solution of $Na_2CO_3(aq)$ (CAS No. 497-19-8). The sodium carbonate solution was made by heating and dissolving 5.2865 g in 997.0 mL of DD water to yield a concentration of 50.00 Mm. The HCl stock solution was then titrated with the 50.00 mM sodium carbonate solution using a ValueWare 50 mL burette. Five trials were performed using phenolphthalein indicator (CAS No. 77-09-8). The titration was considered to have reached the endpoint when a light pink color was reached in the HCl solution.

Once the [HCl] had been determined through standardization using sodium carbonate, an ITC experiment similar to the one described in section 2.3 was repeated using an HCl solution diluted from the stock solution by a factor of 103.5 to give the desired concentration of 1.000 mM. During the ITC run, all other parameters including stir rate, injection number, injection volume, temperature, and tris base concentration and volume were held constant with respect to the experiment described in section 2.3.

S2.5 NaOH – HCl titration

Following the successful calibration of the NanoITC instrument from the tris base-HCl titration, an ITC experiment was performed with sodium hydroxide in place of tris base in order to observe the thermodynamic characteristics of the reaction. The first trial of this experiment involved the titration of 10 different 1.01 μL injections of 60.00 mM HCl, diluted from the previously discussed standardized stock solution into 3.00 x 10^2 μL of a 1.000 mM solution of sodium hydroxide while stirring at a stir rate of 250 RPM at 25 °C. The experiment was repeated, this time with 20 different 1.01 μL injections of 30.00 mM HCl, with all other parameters held constant. Data was modelled using the independent binding style.

S2.6 Streptavidin – Biotin experiment

An experiment was designed for the streptavidin tetramer to bind to a single molecule of biotin with the expected stoichiometry of about 4:1. The experiment was designed for use with a 3.00 x 10^2 μL sample cell volume, a 50 μL titrant volume, and a stir rate of 250 RPM at 25 °C. With the expected stoichiometric ratio of 4 molecules of biotin to one molecule of streptavidin, and the volume of streptavidin in the sample cell being 6 times larger than the volume of biotin in the burette, the biotin was prepared with

a concentration such that it was about 50 times larger than the streptavidin concentration, so that the expected stoichiometry of n ≈ 4 would be indicated at around the midpoint of the reaction.

Streptavidin and biotin solutions discussed in recent literature both require the use of phosphate buffered saline (PBS) as the solvent. Consequently, a solution of 10xPBS (0.1M) buffer was prepared by dissolving 10.9 g of anhydrous sodium phosphate dibasic from Acros Organics (CAS: 7558-79-4, Lot No. B00M2681B), 3.2 g of anhydrous sodium phosphate monobasic from Sigman Chemical Co. (CAS: 7558-80-7, Lot No. 45H02672), and 90 g of sodium chloride from Mallinckrodt Chemicals (CAS: 7647-14-5, Lot No. E42589) in just under 1L of DD H_2O. The pH was then adjusted to about 7.5 and diluted by a factor of 10 to yield a 1xPBS (0.01M) buffer solution.

A 0.5 mL Streptavidin, Alexa Fluor^{TM} 488 conjugate stock solution (2mg/mL) in PBS buffer from Thermo Fisher Scientific (Lot No. 1977355) was used for preparation in the sample cell. Using the reported molecular mass of streptavidin, 55 kDa, the concentration of the stock solution was determined to be 36.36 μM. The stock solution of streptavidin was then diluted to 1.60 μM by diluting by a factor of 18.18 into 1xPBS buffer. Following these steps, a stock solution of Biotin was prepared from Biotin powder (CAS: 58-85-5) from Alfa Aesar (Lot No. T12D027). The biotin solution was prepared by measuring 2.70 mg and dissolving in 30.00 mL of 1xPBS buffer to yield a concentration of 368 μM. The resulting solution was then diluted to 96.0 μM by diluting by a factor of 3.83. The biotin and streptavidin solutions were then both stored in a refrigerator and wrapped in aluminum until use according to the manufacturer's recommendations. An ITC experiment was performed by injecting 15 different 3.33 μL

aliquots of 96.0 μM biotin into 3.00 x 10^2 μL of 2 μM streptavidin while stirring at a stir rate of 250 RPM at 25 °C. Collected data was modelled using the independent binding style.

S2.7 Adenosine Phosphates and RNase A

Following the streptavidin – biotin experiment, a second attempt at measuring protein-ligand binding was performed with RNase A and adenosine phosphates. RNase A reportedly binds to cytidine monophosphate (CMP) with markedly different binding affinities based on the position of the phosphate group.[60] Specifically, 2'-CMP was reported to bind to RNase A with a binding affinity constant of $1x10^6 \, M^{-1}$, while 5'-CMP was reported to bind very weakly, with a binding affinity constant of less than $10^4 \, M^{-1}$. The study suggests that ligands with binding affinities in this range must be determined by ligand exchange experiments. In such experiments, a strongly binding ligand is injected into a prebound solution of macromolecule that has been previously titrated with the weaker binding ligand. As the titration proceeds, the stronger ligand replaces the weaker ligand and the binding constant of the latter can then be accurately calculated.[61]

To adapt this methodology to our project, and to attempt to produce a model suitable for future polymer experimentation, we decided to answer two essential questions: (1) Can we measure ligand exchange in a similar fashion to the steps mentioned above, and (2) What is the effect of the ionic strength? Buffer strength has been reported to be of importance in regards to the binding strength and enthalpy of protein-ligand interactions, especially when metals are involved.[62, 63] One of our goals in this section of this project was to test the effect of buffer concentration on stoichiometry, enthalpy and binding affinity.

An initial test of a strongly binding ligand in the form of 960 µM adenosine-5'-triphosphate disodium salt, 98% (ATP, CAS: 34369-07-8) from Alfa Aesar (LOT: X14F017) was injected into 300 µL of 200 µM RNase A (CAS: 9001-99-4). Both solutions were diluted in 0.15 mM acetate buffer. Twenty-five injections of 2.02 µL aliquots of injectant were performed at 300 s intervals at a stir rate of 250 RPM. The same experiment was repeated using 960 µM adenosine-5'-monophosphate disodium salt (AMP, CAS: 4578-31-8) from Alfa Aesar (LOT: X20G025) with all other parameters held constant. Blank runs were carried out and subtracted from each trial before data analysis was performed. Following these ITC experiments, a ligand exchange test was carried out by injecting ATP into RNase A that had been prebound with AMP. In concordance with traditional standard operating procedure for these types of tests, RNase A was bound to AMP such that ~50% of the active binding sites were prebound before injection of ATP.[61] Thus, the concentration of AMP in the prebound solution of RNase A was 100 µM. This prebound RNase A was used as the sample cell material in an ITC experiment with the same parameters listed above.

A test of ionic strength was performed by repeating the initial test of 960 µM ATP injected into 300 µL of 200 µM RNase A using different concentrations of acetate buffer. In addition to the initial concentration of 0.15 mM, the same experiment was also conducted by diluting the solutions in 0.167 µM and 1.5 mM acetate buffer. Blank runs were also carried out and subtracted for each of these tests preceding data analysis. All experiments in this section were conducted at 25 °C.

S2.8 NanoITC low volume instrument cleaning

To ensure the accuracy of the results from ITC experimentation, a harsh cleaning method was applied to the NanoITC Low Volume instrument. The cleaning procedure was followed according to instructions received via correspondence with technical support chemists at TA Instruments. A cleaning mixture containing 5% v/v Contrad-70 (Decon Labs, CAT# 1002), 20% methanol, and 1M NaOH was prepared in deionized water. A 500 µL aliquot of the mixture was loaded into the sample cell and pipetted up and down 10 times to agitate the solution before removal. A 4N NaOH solution (J.T. Baker Batch No. 0000063841, CAS: 1310-73-2) was then loaded into the sample cell and the temperature of the instrument was set to 65 °C for 60 minutes. The instrument was then allowed to cool back to 25 °C before rinsing with 500 mL of deionized water. A 50% formic acid solution (Honeywell, Lot no. I1710, CAS: 64-18-6) was then loaded into the sample cell, and the temperature of the instrument was then once again set to 65 °C for 60 minutes. The instrument was allowed to cool back to 25 °C and was then rinsed once again with deionized water. Following instrument cleaning, the titration burette was cleaned by back filling with a solution of 0.5% v/v Contrad-70 and pushing the liquid out with the plunger five times. This step was then repeated ten times using deionized water. As described in the following section, titrations of HCl injected into NaOH were performed before any cleaning, after instrument cleaning, and after instrument and titration burette cleaning. Results of these experiments were analyzed to determine the effectiveness of the harsh cleaning methods.

S2.9 HCl NaOH acid/base titrations

An acid/base titration experiment, where 25 injections of 2.02 uL of 30.0 mM HCl were made into 300 uL of 5.68 mM NaOH at 25 °C while stirring at a rate of 250 RPM, was first conducted in January 2021. Following several uses of the NanoITC instrument for various other reactions, the experiment was repeated in July 2021. After obtaining results that varied significantly from those obtained from the original January experiment, the instrument was cleaned and the experiment was repeated to test the effectiveness of the cleaning method. This experiment was also used as a way of determining how often the instrument needed to be cleaned, by repeating the experiment after the use of other reagents such as poly (vbTMAC), NaFL, ATP, RNase A, etc.

S2.10 ATP-RNase A binding

In an initial protein-ligand binding experiment, first conducted in March 2021, 960 µM adenosine-5'-triphosphate disodium salt, 98% (ATP, CAS: 34369-07-8) from Alfa Aesar (LOT: X14F017) was injected into 300 µL of 200 µM RNase A (CAS: 9001-99-4). Both solutions were diluted in 0.15 mM acetate buffer. Twenty-five injections of 2.02 µL aliquots of injectant were performed at 300 s intervals at a stir rate of 250 RPM. This experiment was repeated in July 2021 before and after the harsh cleaning method described in section S2.8 Results were analyzed to test the effectiveness of the harsh cleaning method.

S2.11 NaFL binding to poly (vbTMAC)

An experiment was conducted where twenty-five 2.02 uL aliquots of 9.599 mM Fluorescein disodium salt were injected at 300 s intervals into 300 uL of 10.00 mM poly (vbTMAC) at 25 °C while stirring at 250 RPM. The original experiment was

conducted in April 2021 and was then repeated after the harsh cleaning method in

July 2021. Results were analyzed to ensure the accuracy of the results obtained from

the experiment, and to ensure that the instrument was working properly.

S3: RESULTS

S3.1 Water-water titration

Analysis of titration of DD water into DD water showed that the NanoITC instrument was working properly due to the work of friction from the experiment being detectable at about 0.2 µW. As shown in figure S2, each thermogram reached about 0.20-0.25 µW, and integrated heat areas ranged from -7.3 to -5.6 µJ. A sinusoidal noise of about ± 10 nW was observed during data collection, which signified satisfactory baseline
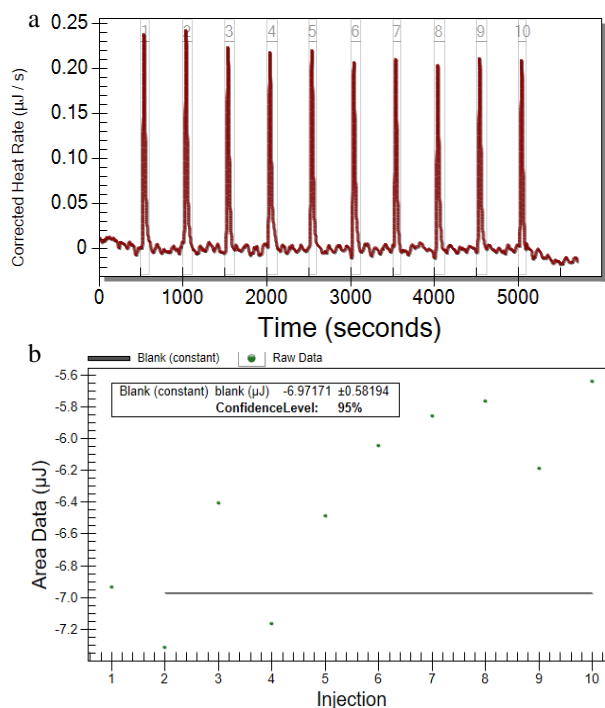

Figure S1: Water-Water titration data.
Heat Rate vs. Time (a) and Integrated
Area vs. Injection Number (b).

stability of the instrument. The data was modelled using the Blank (constant) style and the heat per injection was determined to be -6.97 ± 0.58 µJ. All uncertainties represent 95% confidaence interval.

S3.2 Tris Base – HCl titration

Prior to standardization of the HCl stock solution, the results from the calibration

experiment where excess tris base was titrated with 1.000 mM HCl (Trial 1) showed an

enthalpy value that was slightly too high. The enthalpy of protonation in J/mol at any

temperature between 5 and 50 °C is given as $\Delta H_{protonation} = -49659 + 102.28T -$

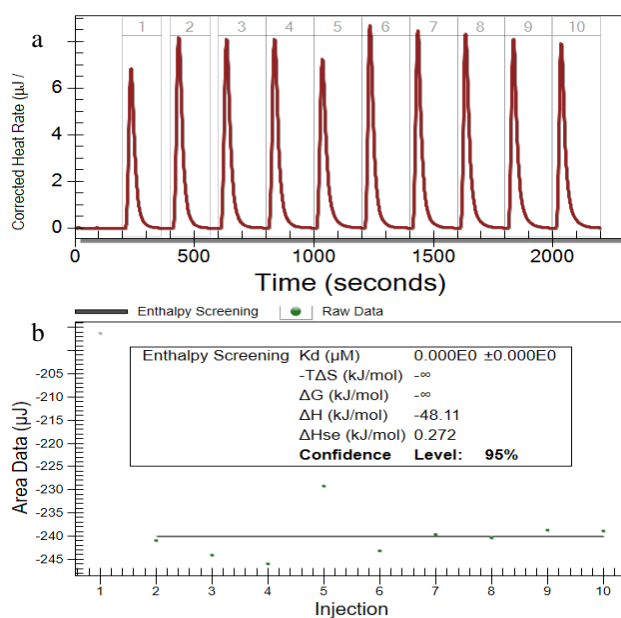$0.59275T^2$. For 25 °C, this value is -47472 J mol^{-1} or -47.472 kJ mol^{-1}. The results for the

Figure S3: ITC data from trial 1 of
excess tris base titrated with 1.000 mM
HCl. $\Delta H_{protonation} = -48.11$ kJ mol^{-1}.

titration of excess tris base with 1.00mM HCl are shown in figure S3. The enthalpy of

protonation was -48.11 kJ mol^{-1}, which indicated that the calibration factor of the

instrument is too high and needed to be reduced.

Following standardization of the HCl stock solution and repeating the experiment,

the results changed slightly to reveal a more positive enthalpy of protonation value. The

results from trial 2 of the tris base-HCl titration experiment, shown in figure S4, reveal

that the calibration factor was, in fact too low to begin with and needed to be increased, as the enthalpy of protonation was -43.19 kJ mol⁻¹, which is less released heat than the expected value of -47.472 kJ mol⁻¹.
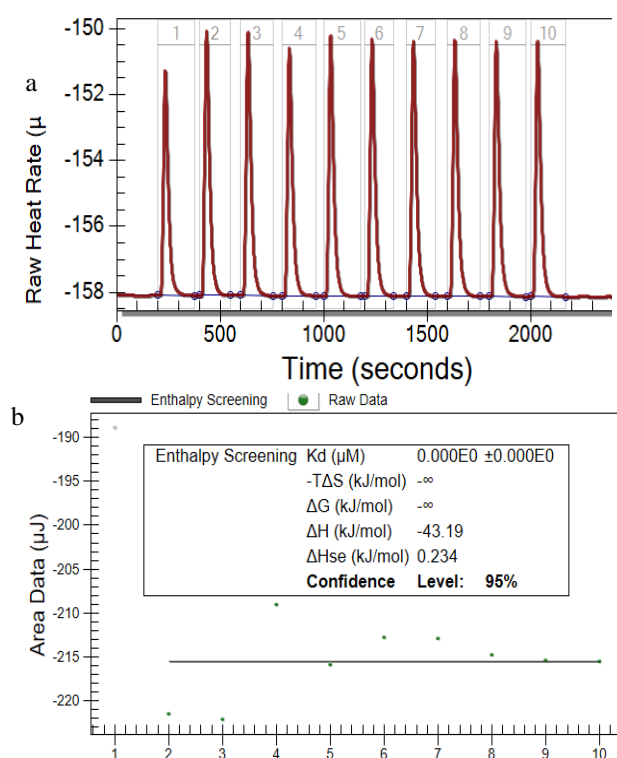

Figure S4: Trial 2 of excess tris base titrated with 1.000 mM HCl. $\Delta H_{protonation} =$ -43.19 kJ mol⁻¹.

A Grubb's test was performed on the integrated area values for each of the nine thermograms produced from the experiment and found that none of the data points should be omitted. Following this experiment, a new calibration factor was determined using the formula: C.F. = (Expected Heat / Measured Heat) x Existing Calibration Factor. Using the existing calibration factor of the instrument, -0.96394, the new calibration factor was determined to be -1.05977. This new calibration factor was entered into the settings of the NanoITC instrument and was used for all future experiments.

S3.3 NaOH – HCl titration

60.00 mM HCl was injected into 1.000 mM NaOH so that the ≈ 1:1 mole ratio
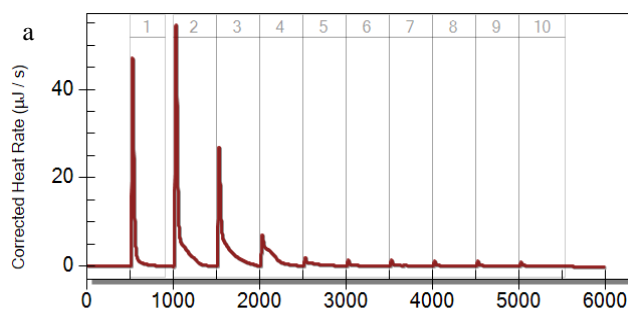

Figure S5: Trial 1 of NaOH – HCl injections. 60.0mM HCl titrated into 1.000 mM NaOH.

would occur at injection #5, where the number of moles of each reagent would be ≈ 3 x

10^{-7} mol. This assumed that the reagent would react in a 1:1 stoichiometric ratio. The

stoichiometry (n) was shown to be about 0.6 over the course of both trials. Figure S5

shows the baseline data for the first trial. During the experiment, some of the

thermograms were not reaching the baseline after post-injection equilibration. Typically,

this is fixed by resetting the instrument and allowing ample time for re-equilibration.

Analysis of experimental results showed that ΔH = -37.99 kJ/mol. Trial 2 of this

experiment was carried out similarly using a lower concentration of HCl. Figure S6

shows the heat rate vs. time and modelled data for the titration of 20 different 1.00 µL

injections 30.00 mM HCl into 3.00 x 10^2 µL of 1.000 mM NaOH. As shown in figure

S6b, the ΔH changed to -45.54 kJ/mol, indicating that more energy was released per mole
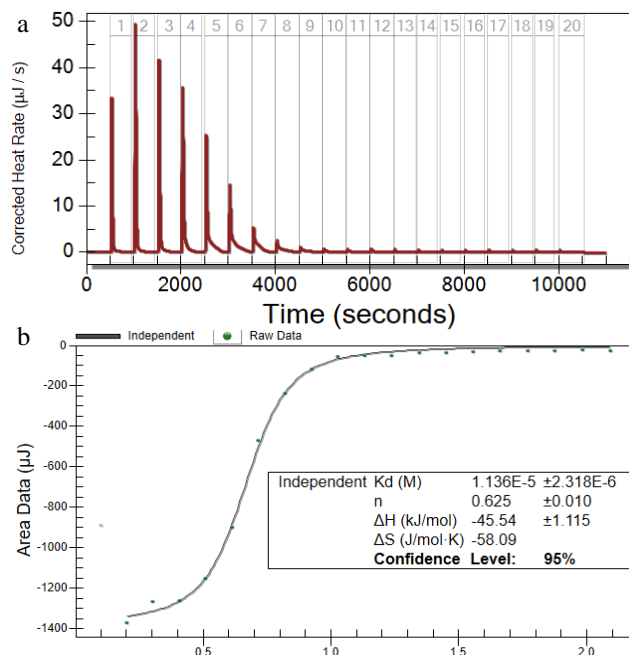
of HCl relative to the previous experiment.

a

b

Independent	Kd (M)	1.136E-5	±2.318E-6
	n	0.625	±0.010
	ΔH (kJ/mol)	-45.54	±1.115
	ΔS (J/mol·K)	-58.09	
	Confidence Level:		**95%**

Figure S6: 30.00 mM HCl titrated into
1.000 mM NaOH.

S3.4 Streptavidin – Biotin experimentWith the ultimate goal in mind of characterizing

polymer binding interactions, a model experiment using protein-ligand binding needed to

first be produced. For this model, we attempted to recreate the interaction of biotin

binding to streptavidin that has been reported in recent literature.[64-66] Previous work on

the binding characteristics of streptavidin and biotin indicated through the use of ITC that

the binding affinity of streptavidin is extremely high ($K_d \approx 10^{-14}$) and that the

stoichiometry of the reaction occurs at approximately 1:1 with the streptavidin monomer

binding to biotin at 25 °C. Our results show the interaction of the streptavidin tetramer
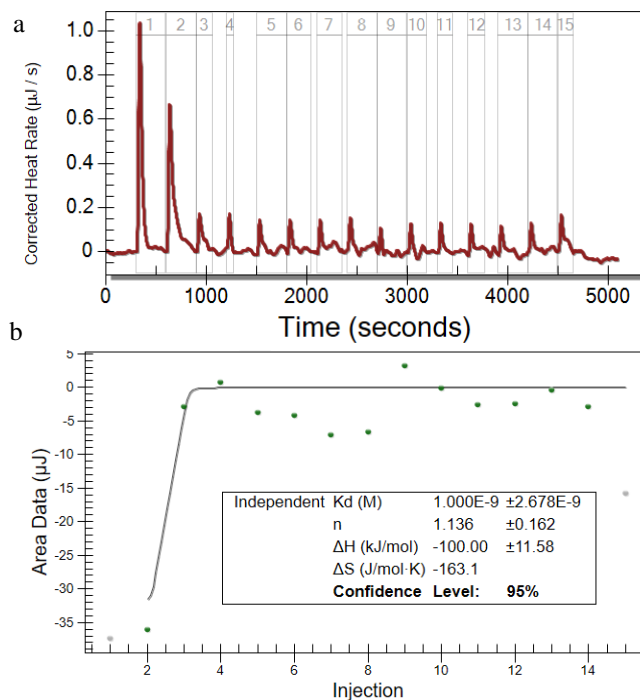
interacting with biotin in figure S7.

Figure S7: ITC data from 2 µM Streptavidin binding to 96 µM biotin through 15 injections of 3.33 µL aliquots.

S3.5 Adenosine Phosphates and RNase A

Campoy and Freire showed that binding affinity constant, K_a values less than 10^4 M^{-1} indicate weakly binding ligands, while those that are above 10^8 M^{-1} indicate strongly binding ligands,[61] whereas if 10^4 $M^{-1} < K_a < 10^8 M^{-1}$, the ligand can be considered to have moderate binding strength. Our initial experiment of 960 µM ATP injected into 200 µM RNase A revealed that ATP exhibits moderate binding, with a K_a value of 4.963×10^6 M^{-1}. The molar enthalpy of the 5'-ATP binding to RNase A (-85.12 kJ/mol) was greater than the molar enthalpy reported for 2'-CMP (-65kJ/mol), most likely due to the increase in the number of phosphate groups.[60] The results for the original ATP – RNase A experiment are shown in figure S8.
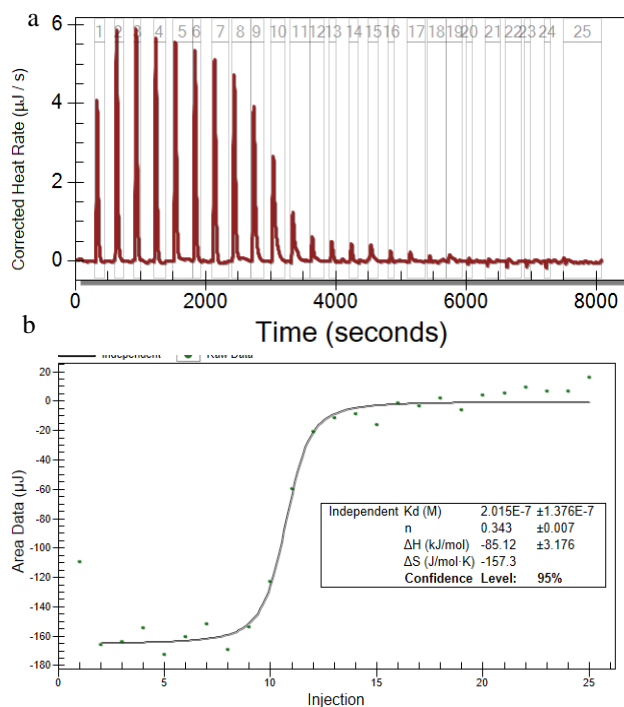
Figure S8: 960 µM ATP binding to 200 µM RNase A through 25 injections of 2.02 µL aliquots. $K_a = 4.963 \times 10^6$ M^{-1}. $\Delta G = -38.22$ kJ/mol. $\Delta S = -157.3$ J/molK.

The ATP - RNase A titration was repeated at different ionic strength solutions such as 0.167 µM (the smallest possible), 0.15 mM and up to 1.5 mM. Within 95% confidence intervals, the buffer strength did not have a significant effect on binding affinity, enthalpy, and stoichiometry. Figures S9 and S10 show the results of the ATP – RNase A titration using 0.167 µM and 1.5 mM acetate buffer, respectively.
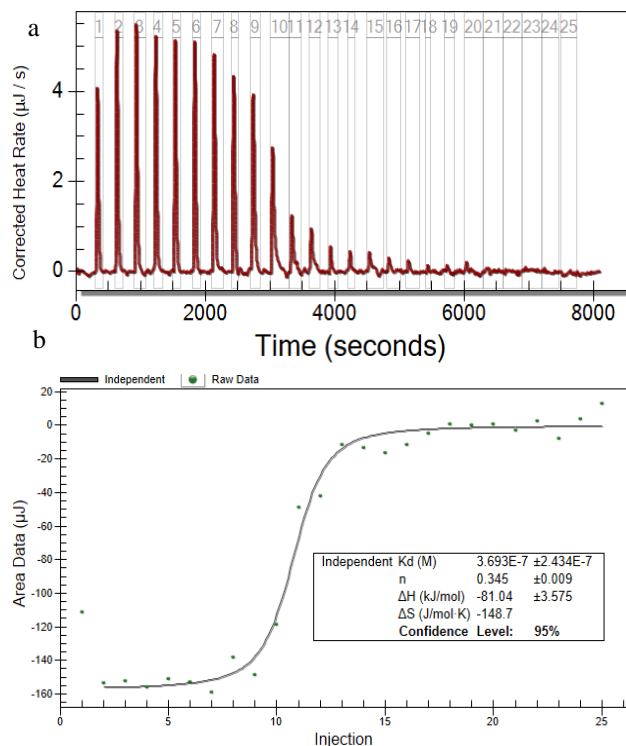
Figure S9: 960 µM ATP binding to 200 µM RNase A through 25 injections of 2.02 µL aliquots. 0.167 µM acetate buffer. $K_a = 2.708 \times 10^6$ M^{-1}. $\Delta G = -36.72$ kJ/mol. $\Delta S = -148.7$ J/molK.
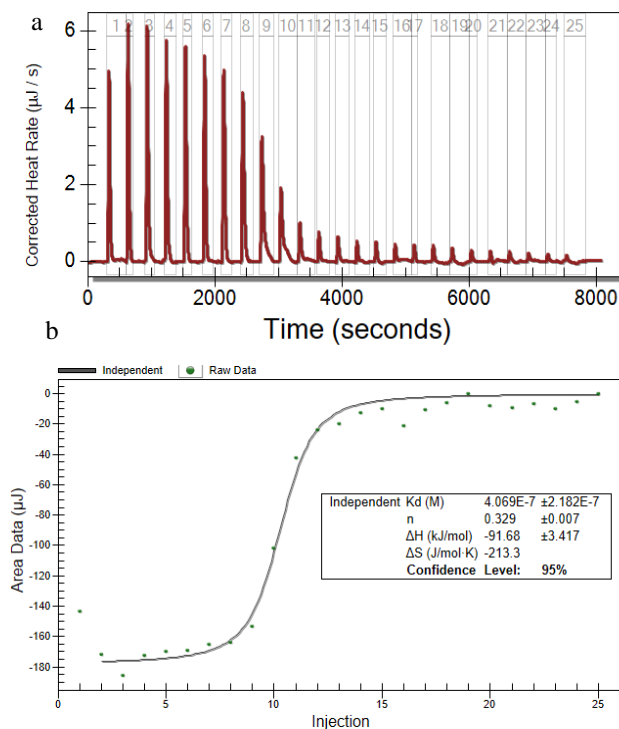
Figure S10: 960 µM ATP binding to 200 µM RNase A through 25 injections of 2.02 µL aliquots. 1.5 µM acetate buffer. $K_a = 2.457 \times 10^6$ M^{-1}. $\Delta G = -36.48$ kJ/mol. $\Delta S = -185.1$ J/molK.

Following the analysis of ATP binding, AMP was used to compare results using a weaker binding ligand to RNase A. Figure S11 shows the results of this test. All parameters from the original ATP – RNase A experiment were held constant. As expected, the binding affinity of AMP binding to RNase A was much lower ($K_a = 6.400 \times 10^4$ M^{-1}) than that of ATP. The molar enthalpy, ($\Delta H = -44.38$ kJ/mol) was also less than that of the ATP. When comparing the binding of AMP and ATP to RNase A, the stoichiometry seemed to be about the same, each slightly greater than 0.33.

A ligand exchange test was carried out by first binding 50% of the active binding sites of RNase A with AMP. The prebound RNase A was then used as the sample cell material
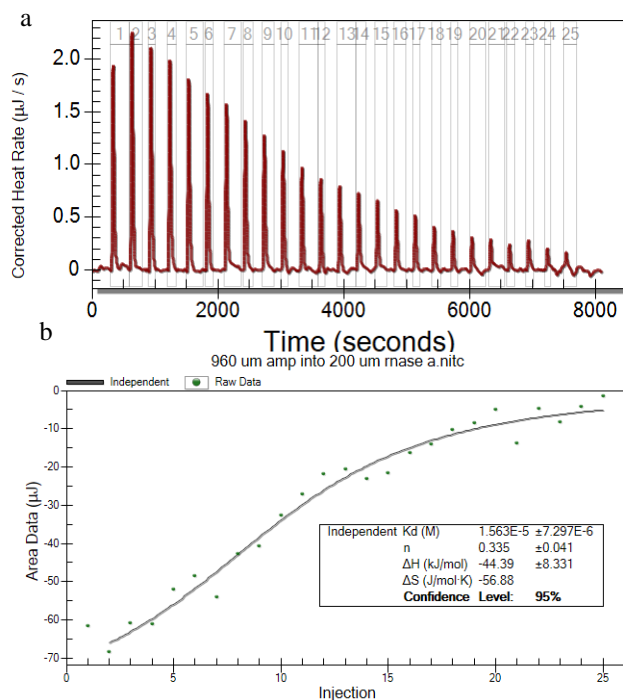
Figure S11: 960 μM AMP binding to 200 μM RNase A through 25 injections of 2.02 μL aliquots. 0.15 μM acetate buffer. $K_a = 6.400 \times 10^4$ M^{-1}. $\Delta G = -27.43$ kJ/mol. $\Delta S = -56.84$ J/molK.

and injected with ATP. As shown in figure S12, the binding affinity and molar enthalpy

of this experiment both fell in-between the values that were obtained for AMP and ATP,

indicating that competitive binding was taking place. K_a for this experiment was 5.779 x

10^5 M^{-1} and ΔH was -68.22 kJ/mol. Interestingly, stoichiometry seemed to remain the

same, at about 0.34.

a

b

960 um atp into 200 um rnase a prebound with 100 um amp..nitc

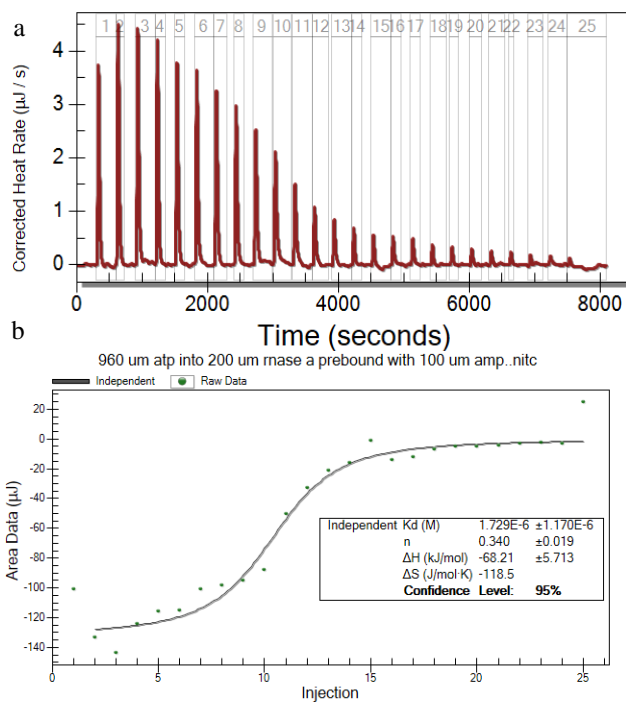| Independent Kd (M) | 1.729E-6 | ±1.170E-6 |
n	0.340	±0.019
ΔH (kJ/mol)	-68.21	±5.713
ΔS (J/mol·K)	-118.5	
Confidence Level:	**95%**	

Figure S12: 960 µM AMP binding to 200 µM RNase A prebound with 100 µM AMP. $K_a = 5.779 \times 10^5$ M^{-1}. ΔG = -32.89 kJ/mol. ΔS = -118.5 J/molK.

S3.6 HCl NaOH titrations pre- and post-cleaning

In the original acid/base titration experiment, a sigmoidal curve is observed in the titration curve beginning at injection 12. Stoichiometry for this reaction was 0.897 ± 0.008, Ka = 1.1E5 ± 4E4 M^{-1}, and ΔH = -52.7 ± 0.95 kJ mol^{-1}. The titration curve and injection plot for this experiment are shown in figure S13. According to the ITC Run
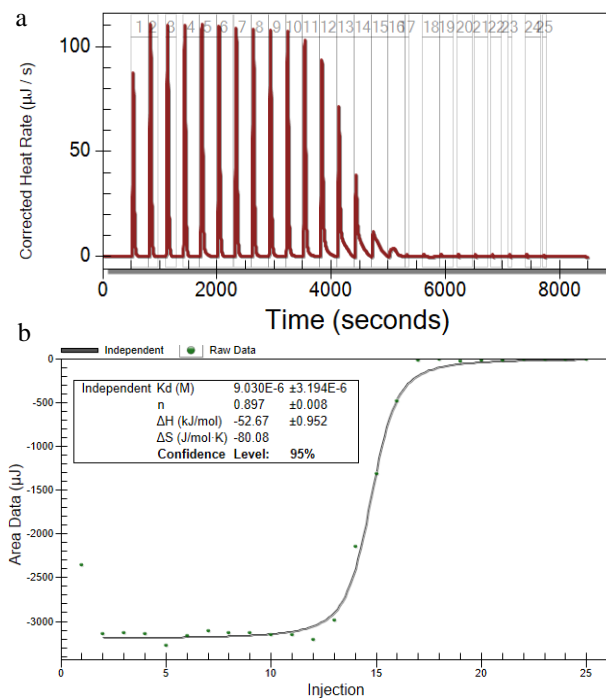

Figure S12: Original NaOH-HCl titration conducted in January 2021. Titration curve (a) and injection plot (b).

Getting Started Guide from TA Instruments, the enthalpy of protonation in J/mol at temperatures between 5 and 50°C is: ΔH$_{protonation}$ = -49659 + 102.28T - 0.59275T^2

At 25.0000 °C, the expected value of enthalpy of protonation is -47472 J mol^{-1} or -47.472 kJ mol^{-1}. The enthalpy value for the original HCl-NaOH experiment was therefore slightly higher than expected. It is also noteworthy that the binding association constant value estimated by the modelling software for this experiment was on the order of 10^5 M^{-1}. One might expect that, because the reaction of HCl and NaOH should favor

virtually completely the formation of products, the Ka value estimated for this reaction would be the largest value that could be accurately estimated by the modelling software, which would be about 10^8 M^{-1}.

The HCl-NaOH titration experiment was repeated in July 2021 before applying the harsh cleaning method, after cleaning the instrument and then again after cleaning the titration syringe. Results for these experiments are shown in figures S14, S15 and S16, respectively. Before cleaning the instrument, the July results of this experiment were as follows: Ka = 5E3 ± 2E3 M^{-1}, n = 0.481 ± 0.025, and ΔH = -43 ± 3.5 kJ mol^{-1}. Here, it is shown that the association constant value estimated for this reaction is two orders of magnitude lower than that of the original January experiment. The observation was also made that the titration curve in figure S14a lacks the sigmoidal curve shape that is present in figure S13. Additionally, it was observed that the stoichiometry was about half that of
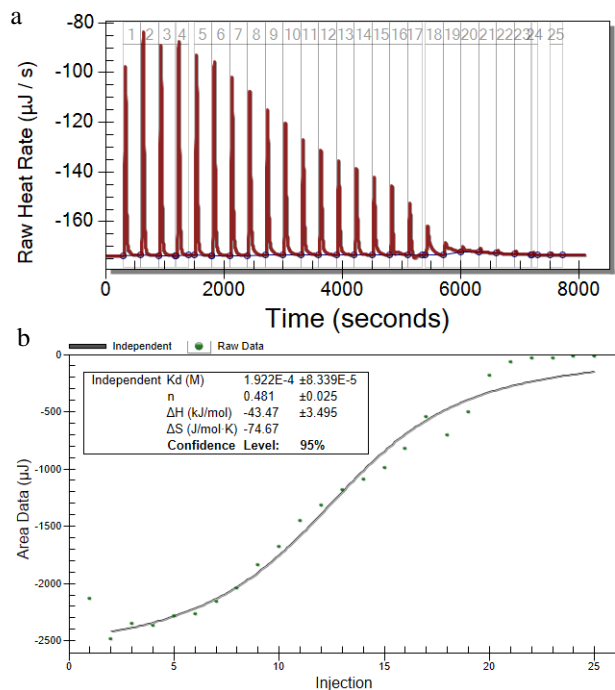

Figure S14: July HCl-NaOH titration experiment before cleaning. Titration curve (a) and injection plot (b).
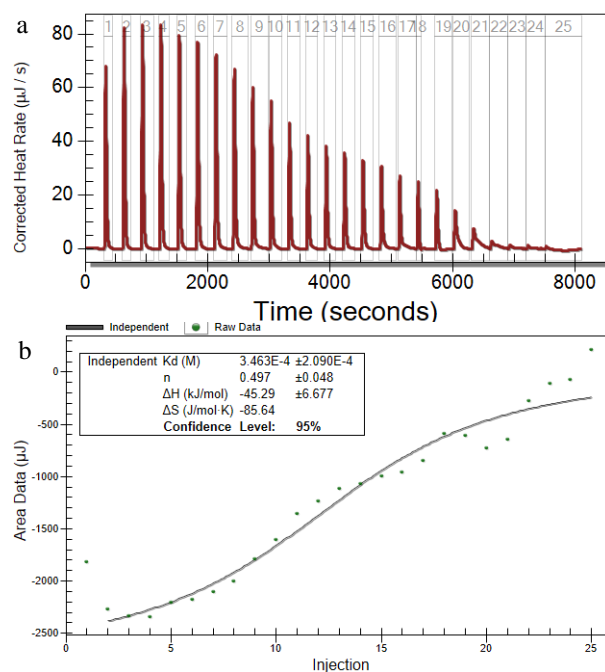
Figure S15: July HCl-NaOH titration experiment after cleaning the instrument. Titration curve (a) and injection plot (b).
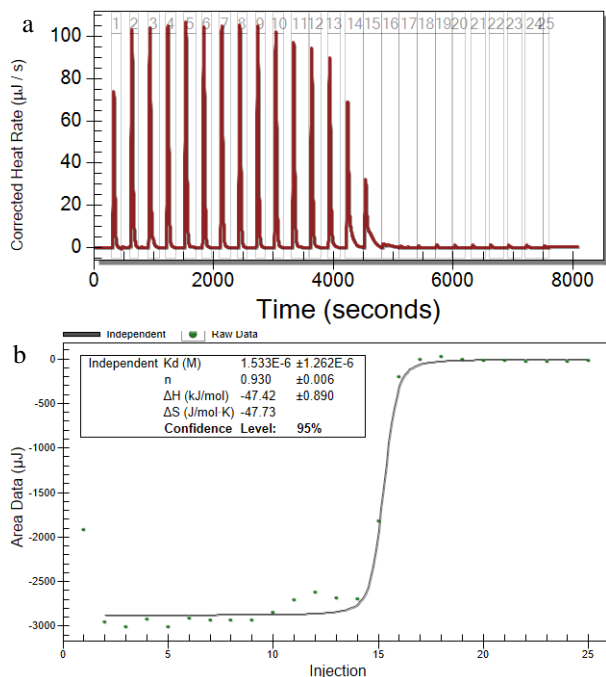
Figure S13: July HCl-NaOH titration experiment after cleaning the instrument and the titration burette. Titration curve (a) and injection plot (b).

the original January experiment. These observations served as evidence of the fact that the instrument was not working properly and needed to be cleaned before conducting any further experiments.

After applying the harsh cleaning method to the instrument, but not the titration burette, the HCl-NaOH experiment was repeated. Shown in figure S15, results were as follows: $Ka = 3E3 \pm 1.7E3$ M^{-1}, $n = 0.497 \pm 0.048$, and $\Delta H = -45 \pm 6.7$ kJ mol^{-1}. While these results were consistent with the results from the pre-cleaning experiment, they were still not consistent with the January results, indicating that the titration burette also needed to be cleaned before further experimentation.

Following these experiments, the titration burette was cleaned according to the procedure described in section S2.8. The experiment was repeated a final time, after cleaning the instrument and the titration burette. Results for this experiment, shown in

figure S16, are as follows: Ka = 7E5 ± 5.5E5 M^{-1}, n = 0.930 ± 0.006, and ΔH = -47.4 ±

0.89 kJ mol^{-1}. As is evidenced by the Ka value and the presence of the sigmoidal curve

beginning at injection 12, this experiment more closely matches the January experiment

than those conducted prior to cleaning the instrument and the burette. It is also

noteworthy that the estimated enthalpy of protonation value for the post-cleaning

experiment matches the expected value from the Getting Started Guide, mentioned

above. These observations support the conclusion that the instrument had been cleaned

and was now working properly.

S3.7 ATP-RNase A binding pre- and post-cleaning

An original protein-ligand binding experiment was conducted in February. The

results for the original February experiment are as follows: Ka = 5E6 ± 4E6 M^{-1}, n =

0.342 ± 0.008, and ΔH = -86 ± 4 kJ mol^{-1}. The titration curve and injection plot for this
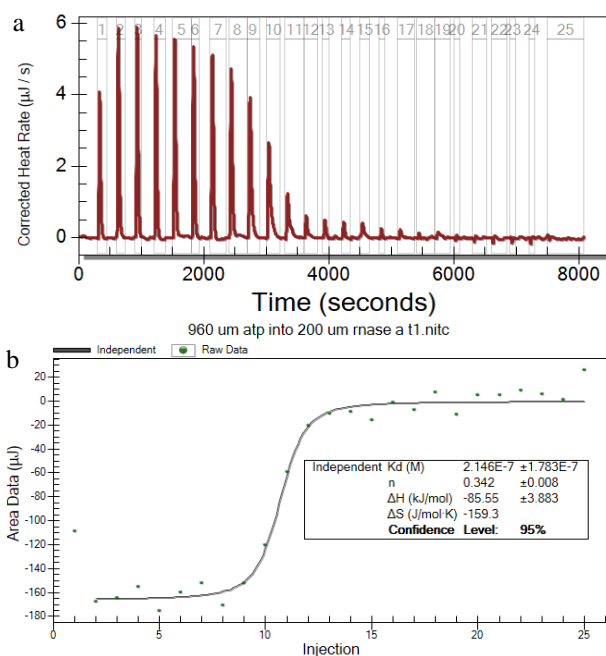

Figure S14: Original February ATP-RNase A experiment. Titration curve (a) and injection plot (b).

experiment is shown in figure S17. This experiment was then repeated in July before and after cleaning. Titration curve and injection plot data for the pre- and post-cleaning tests are shown in figures S18 and S19, respectively. Results for the July pre-cleaning experiment are as follows: $Ka = 4E5 \pm 1E5$ M^{-1}, $n = 0.495 \pm 0.013$, and $\Delta H = -81 \pm 3$ kJ mol^{-1}. Results for the July post-cleaning experiment are as follows: $Ka = 1.3E6 \pm 6E5$ M^{-1}, $n = 0.332 \pm 0.009$, and $\Delta H = -82 \pm 3.6$ kJ mol^{-1}.
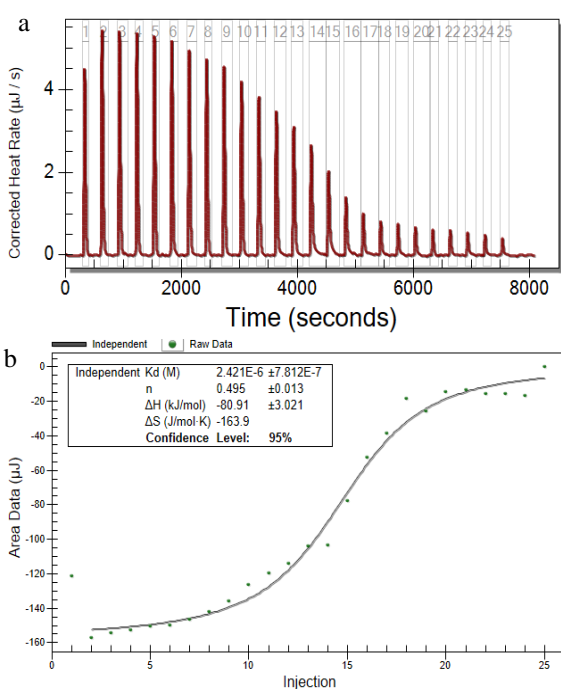
Figure S16: July ATP-RNase A experiment before instrument cleaning. Titration curve (a) and injection plot (b).
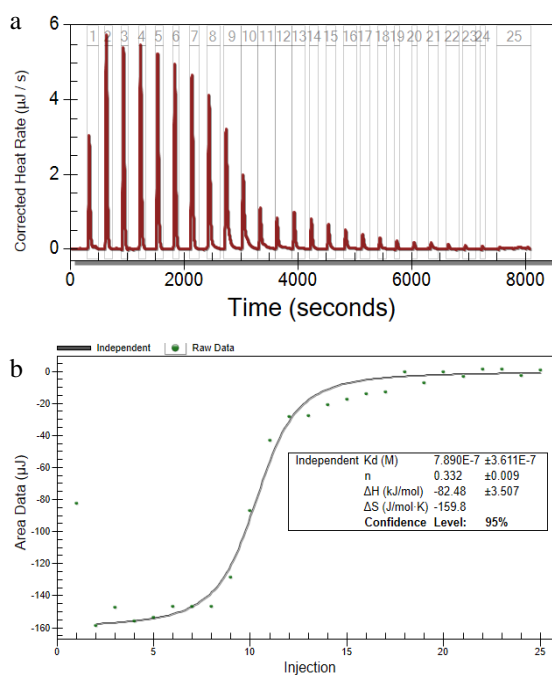
Figure S15: July ATP-RNase A experiment after instrument cleaning. Titration curve (a) and injection plot (b).

For all three estimated parameters, the post-cleaning experiment data matched that of the original February experiment within a 95% confidence interval, while the pre-cleaning experiment data differed greatly. From these data, it can be concluded that the cleaning procedure was effective at restoring the instrument to its former accuracy.

S3.8 NaFL binding to poly (vbTMAC) pre- and post-cleaning

An experiment where NaFL was injected into poly (vbTMAC) was conducted in April. Results for the original April experiment, shown in figure S20, are as follows: Ka = 8E3 ± 5E3 M^{-1}, n = 0.107 ± 0.008, and ΔH = -10 ± 1.3 kJ mol^{-1}. The experiment was conducted again after cleaning the instrument and the burette. Results for the post cleaning experiment, shown in figure S21, are as follows: Ka = 5E3 ± 9E3 M^{-1}, n = 0.100 ± 0.001, and ΔH = -17 ± 6 kJ mol^{-1}.
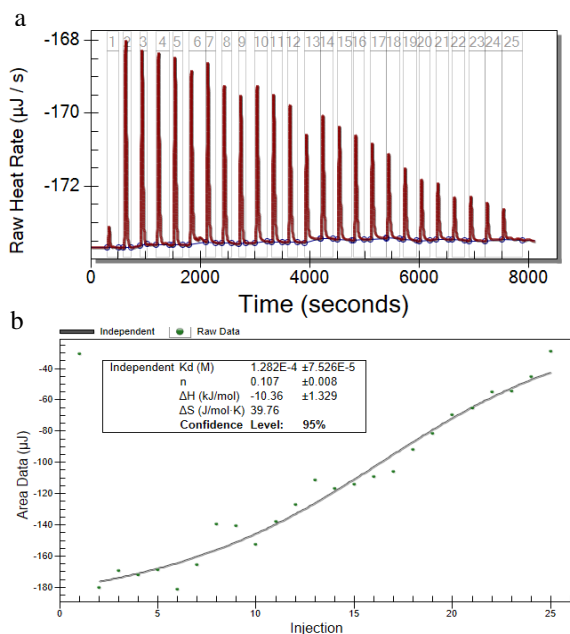
Figure S7: Original April experiment – NaFL injections into poly (vbTMAC). Titration curve (a) and injection plot (b).

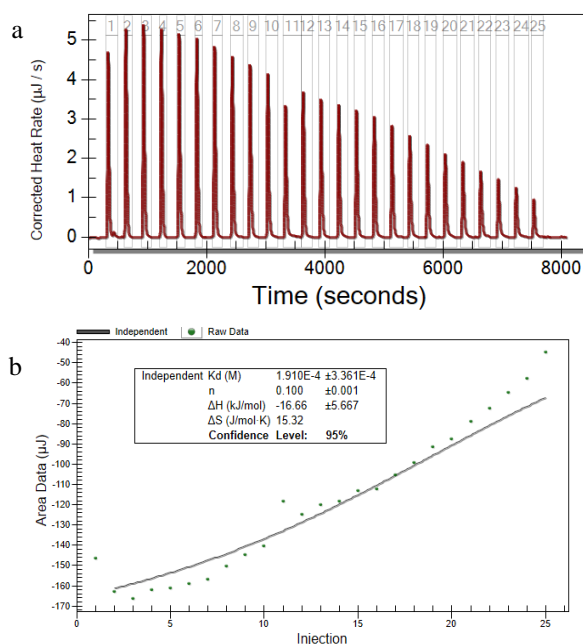Figure S8: Post-cleaning experiment – NaFL injections into poly (vbTMAC). Titration curve (a) and injection plot (b).

Because each of the estimated parameters did not change before and after cleaning, it can be concluded that the instrument's cleanliness did not influence the accuracy of the results. These data suggest that the binding interaction of NaFL binding to unfunctionalized poly (vbTMAC) is a weak binding interaction.

S4: CONCLUSIONS

Preliminary work in this project has revealed that ITC is useful for measuring binding affinity and accessibility of binding sites for protein-ligand binding interactions. After passing some early roadblocks and understanding more about the limitations of the instrumentation, we were able to obtain a working model for protein-based binding experimentation. We learned that baseline stability is critical to achieving reliable data, and that proper calibration is necessary for accuracy of results. Ionic strength, though an important parameter to consider for metal binding analysis, did not have a significant effect on protein - ligand binding for reactions that do not involve metals.

Our ultimate objective is the thermodynamic characterization of the binding of poly (vinyl benzyl trimethylammonium chloride) (poly(vbTMAC)) to several contaminants including those mentioned above. We also plan on changing the polymer strand length from 10-1000 monomers and testing the effect on the binding site accessibility. Our expectations are that the binding site accessibility will decrease as a function of increasing polymer strand length due to folding of the polymer. Future steps in this project involve the grafting of our polymer onto such scaffoldings such as cellulose, fluorographene, and zeolite, and characterizing the binding interactions to known drinking water contaminants by ITC.

REFERENCES

1.   Abouzeid, R. E.; Khiari, R.; El-Wakil, N.; Dufresne, A., Current State and New Trends in the Use of Cellulose Nanomaterials for Wastewater Treatment. *Biomacromolecules* **2019,** *20* (2), 573-597.

2.   Klemm, D.; Schumann, D.; Kramer, F.; Heßler, N.; Hornung, M.; Schmauder, H.-P.; Marsch, S., Nanocelluloses as Innovative Polymers in Research and Application. Springer Berlin Heidelberg: 2006; pp 49-96.

3.   Li, Q.; Chen, G.; Xing, T.; Miao, S., Dry transfer printing of silk and cotton with reactive dyes and mixed polysaccharide thickeners. *Coloration Technology* **2018,** *134* (3), 222-229.

4.   Obele, C. M.; Ibenta, M. E.; Chukwuneke, J. L.; Nwanonenyi, S. C., Carboxymethyl cellulose and cellulose nanocrystals from cassava stem as thickeners in reactive printing of cotton. *Cellulose* **2021,** *28* (4), 2615-2633.

5.   Bampidis, V.; Azimonti, G.; Bastos, M. D. L.; Christensen, H.; Dusemund, B.; Kos Durjava, M.; Kouba, M.; López-Alonso, M.; López Puente, S.; Marcon, F.; Mayo, B.; Pechová, A.; Petkova, M.; Ramos, F.; Sanz, Y.; Villa, R. E.; Woutersen, R.; Bories, G.; Gropp, J.; Nebbia, C.; Innocenti, M. L.; Aquilina, G., Safety and efficacy of methyl cellulose for all animal species. *EFSA Journal* **2020,** *18* (7).

6.   Perinelli, D. R.; Berardi, A.; Bisharat, L.; Cambriani, A.; Ganzetti, R.; Bonacucina, G.; Cespi, M.; Palmieri, G. F., Rheological properties of cellulosic thickeners in hydro-alcoholic media: The science behind the formulation of hand sanitizer gels. *International Journal of Pharmaceutics* **2021,** *604*, 120769.

7.   Camarero Espinosa, S.; Kuhnt, T.; Foster, E. J.; Weder, C., Isolation of Thermally Stable Cellulose Nanocrystals by Phosphoric Acid Hydrolysis. *Biomacromolecules* **2013,** *14* (4), 1223-1230.

8.   Spinella, S.; Maiorana, A.; Qian, Q.; Dawson, N. J.; Hepworth, V.; McCallum, S. A.; Ganesh, M.; Singer, K. D.; Gross, R. A., Concurrent Cellulose Hydrolysis and Esterification to Prepare a Surface-Modified Cellulose Nanocrystal Decorated with Carboxylic Acid Moieties. *ACS Sustainable Chemistry & Engineering* **2016,** *4* (3), 1538-1550.

9.   Kang, X.; Sun, P.; Kuga, S.; Wang, C.; Zhao, Y.; Wu, M.; Huang, Y., Thin Cellulose Nanofiber from Corncob Cellulose and Its Performance in Transparent Nanopaper. *ACS Sustainable Chemistry & Engineering* **2017,** *5* (3), 2529-2534.

10. Sèbe, G.; Ham-Pichavant, F.; Pecastaings, G., Dispersibility and Emulsion-Stabilizing Effect of Cellulose Nanowhiskers Esterified by Vinyl Acetate and Vinyl Cinnamate. *Biomacromolecules* **2013,** *14* (8), 2937-2944.

11. Ávila Ramírez, J. A.; Fortunati, E.; Kenny, J. M.; Torre, L.; Foresti, M. L., Simple citric acid-catalyzed surface esterification of cellulose nanocrystals. *Carbohydrate Polymers* **2017,** *157*, 1358-1364.

12. Espino-Pérez, E.; Bras, J.; Almeida, G.; Relkin, P.; Belgacem, N.; Plessis, C.; Domenek, S., Cellulose nanocrystal surface functionalization for the controlled sorption of water and organic vapours. *Cellulose* **2016,** *23* (5), 2955-2970.

13. Nguyen, H.; Hsiao, M.-Y.; Nagai, K.; Lin, H., Suppressed crystallization and enhanced gas permeability in thin films of cellulose acetate blends. *Polymer* **2020,** *205*, 122790.

14. Duan, H.; Shao, Z.; Zhao, M.; Zhou, Z., Preparation and properties of environmental-friendly coatings based on carboxymethyl cellulose nitrate ester & modified alkyd. *Carbohydrate Polymers* **2016,** *137*, 92-99.

15. Isogai, A.; Hänninen, T.; Fujisawa, S.; Saito, T., Review: Catalytic oxidation of cellulose with nitroxyl radicals under aqueous conditions. *Progress in Polymer Science* **2018,** *86*, 122-148.

16. O'Connell, D. W.; Birkinshaw, C.; O'Dwyer, T. F., Heavy metal adsorbents prepared from the modification of cellulose: A review. *Bioresource Technology* **2008,** *99* (15), 6709-6724.

17. Aburabie, J.; Lalia, B.; Hashaikeh, R., Proton Conductive, Low Methanol Crossover Cellulose-Based Membranes. *Membranes* **2021,** *11* (7), 539.

18. Jois, H. S. S.; Bhat, D. K., Miscibility, water uptake, ion exchange capacity, conductivity and dielectric studies of poly(methyl methacrylate) and cellulose acetate blends. *Journal of Applied Polymer Science* **2013,** *130* (5), 3074-3081.

19. Qiu, X.; Hu, S., "Smart" Materials Based on Cellulose: A Review of the Preparations, Properties, and Applications. *Materials* **2013,** *6* (3), 738-781.

20. Wang, Y.; Wang, X.; Xie, Y.; Zhang, K., Functional nanomaterials through esterification of cellulose: a review of chemistry and application. *Cellulose* **2018,** *25* (7), 3703-3731.

21. Habibi, Y.; Lucia, L. A.; Rojas, O. J., Cellulose Nanocrystals: Chemistry, Self-Assembly, and Applications. *Chemical Reviews* **2010,** *110* (6), 3479-3500.

22.   Braun, B.; Dorgan, J. R., Single-Step Method for the Isolation and Surface Functionalization of Cellulosic Nanowhiskers. *Biomacromolecules* **2009,** *10* (2), 334-341.

23.   Saito, T.; Hirota, M.; Tamura, N.; Kimura, S.; Fukuzumi, H.; Heux, L.; Isogai, A., Individualization of Nano-Sized Plant Cellulose Fibrils by Direct Surface Carboxylation Using TEMPO Catalyst under Neutral Conditions. *Biomacromolecules* **2009,** *10* (7), 1992-1996.

24.   Chen, H.; Li, R.; Xie, J.; Xu, X.; Chen, S., Facile methacrylation of cellulose via alkaline aqueous esterification for thiol–ene click functionalization. *Materials Letters* **2019,** *245*, 18-21.

25.   Nikiforova, T. E.; Kozlov, V. A., Study of the effect of oxidative-bisulfite modification of the cotton cellulose on its ion exchange properties. *Russian Journal of General Chemistry* **2011,** *81* (10), 2136-2141.

26.   Luneva, N. K.; Ezovitova, T. I., Cellulose phosphorylation with a mixture of orthophosphoric acid and ammonium polyphosphate in urea medium. *Russian Journal of Applied Chemistry* **2014,** *87* (10), 1558-1565.

27.   Gurgel, L. V. A.; Perin de Melo, J. C.; de Lena, J. C.; Gil, L. F., Adsorption of chromium (VI) ion from aqueous solution by succinylated mercerized cellulose functionalized with quaternary ammonium groups. *Bioresource Technology* **2009,** *100* (13), 3214-3220.

28.   Isogai, A.; Kato, Y., Preparation of polyuronic acid from cellulose by TEMPO-mediated oxidation. *Cellulose* **1998,** *5* (3), 153-164.

29.   Lu, H.; Behm, M.; Leijonmarck, S.; Lindbergh, G.; Cornell, A., Flexible Paper Electrodes for Li-Ion Batteries Using Low Amount of TEMPO-Oxidized Cellulose Nanofibrils as Binder. *ACS Applied Materials & Interfaces* **2016,** *8* (28), 18097-18106.

30.   Ito, H.; Sakata, M.; Hongo, C.; Matsumoto, T.; Nishino, T., Cellulose nanofiber nanocomposites with aligned silver nanoparticles. *Nanocomposites* **2018,** *4* (4), 167-177.

31.   Luo, W.; Shen, F.; Bommier, C.; Zhu, H.; Ji, X.; Hu, L., Na-Ion Battery Anodes: Materials and Electrochemistry. *Accounts of Chemical Research* **2016,** *49* (2), 231-240.

32.   Juntadech, T.; Nantasenamat, C.; Chitpong, N., Oxidized regenerated cellulose nanofiber membranes for capturing heavy metals in aqueous solutions. *Cellulose* **2021,** *28* (18), 11465-11482.

33.   Kalia, S.; Boufi, S.; Celli, A.; Kango, S., Nanofibrillated cellulose: surface modification and potential applications. *Colloid and Polymer Science* **2014,** *292* (1), 5-31.

34.   Geise, G. M.; Lee, H.-S.; Miller, D. J.; Freeman, B. D.; McGrath, J. E.; Paul, D. R., Water purification by membranes: The role of polymer science. *Journal of Polymer Science Part B: Polymer Physics* **2010,** *48* (15), 1685-1718.

35.   Sharma, A.; Anjana; Rana, H.; Goswami, S., A Comprehensive Review on the Heavy Metal Removal for Water Remediation by the Application of Lignocellulosic Biomass-Derived Nanocellulose. *Journal of Polymers and the Environment* **2021**.

36.   Singh, N.; Wang, J.; Ulbricht, M.; Wickramasinghe, S. R.; Husson, S. M., Surface-initiated atom transfer radical polymerization: A new method for preparation of polymeric membrane adsorbers. *Journal of Membrane Science* **2008,** *309* (1-2), 64-72.

37.   Morits, M.; McKee, J. R.; Majoinen, J.; Malho, J.-M.; Houbenov, N.; Seitsonen, J.; Laine, J.; Gröschel, A. H.; Ikkala, O., Polymer Brushes on Cellulose Nanofibers: Modification, SI-ATRP, and Unexpected Degradation Processes. *ACS Sustainable Chemistry & Engineering* **2017,** *5* (9), 7642-7650.

38.   Nematdoust, S.; Najjar, R.; Bresser, D.; Passerini, S., Partially Oxidized Cellulose grafted with Polyethylene Glycol mono-Methyl Ether (m-PEG) as Electrolyte Material for Lithium Polymer Battery. *Carbohydrate Polymers* **2020,** *240*, 116339.

39.   Benkaddour, A.; Jradi, K.; Robert, S.; Daneault, C., Study of the Effect of Grafting Method on Surface Polarity of Tempo-Oxidized Nanocellulose Using Polycaprolactone as the Modifying Compound: Esterification versus Click-Chemistry. *Nanomaterials* **2013,** *3* (4), 638-654.

40.   Jakubowski, W.; Min, K.; Matyjaszewski, K., Activators Regenerated by Electron Transfer for Atom Transfer Radical Polymerization of Styrene. *Macromolecules* **2006,** *39* (1), 39-45.

41.   Sahu, A.; Alston, J. R.; Carlin, C.; Craps, M.; Davis, K.; Harrison, H. B.; Kongruengkit, T.; Manikonda, A.; Elmore, S.; Rollins, R.; Sadiku, B.; Schmal, S.; Shajahan, J.; Poler, J. C., Fluorographite Nanoplatelets with Covalent Grafting of Anion-Exchange Resins for Water Purification. *ACS Applied Nano Materials* **2022,** *5* (4), 5709-5721.

42.   Sahu, A.; Sheikh, R.; Poler, J. C., Green sonochemical synthesis, kinetics and functionalization of nanoscale anion exchange resins and their performance as water purification membranes. *Ultrasonics Sonochemistry* **2020,** *67*, 105163.

43.   Rickard, B. P.; Rizvi, I.; Fenton, S. E., Per- and poly-fluoroalkyl substances (PFAS) and female reproductive outcomes: PFAS elimination, endocrine-mediated effects, and disease. *Toxicology* **2022,** *465*, 153031.

44.   Von Holst, H.; Nayak, P.; Dembek, Z.; Buehler, S.; Echeverria, D.; Fallacara, D.; John, L., Perfluoroalkyl substances exposure and immunity, allergic response, infection, and asthma in children: review of epidemiologic studies. *Heliyon* **2021,** *7* (10), e08160.

45.   Fraley, K. M.; Fraley, H. N.; Arthur, D.; Walther, E. J., Per- and Polyfluoroalkyl Substances (PFAS): Anglers May Be Exposed to Harmful Chemicals in Their Catch. *Fisheries* **2020,** *45* (3), 138-144.

46.   Annunziato, K. M.; Doherty, J.; Lee, J.; Clark, J. M.; Liang, W. L.; Clark, C. W.; Nguyen, M.; Roy, M. A.; Timme-Laragy, A. R., Chemical Characterization of a Legacy Aqueous Film-Forming Foam Sample and Developmental Toxicity in Zebrafish (Danio rerio). *Environ. Health Perspect.* **2020,** *128* (9), 13.

47.   Maga, D.; Aryan, V.; Bruzzano, S., Environmental Assessment of Various End-of-Life Pathways for Treating Per- and Polyfluoroalkyl Substances in Spent Fire-Extinguishing Waters. *Environ. Toxicol. Chem.* **2021,** *40* (3), 947-957.

48.   Ward, W. H.; Holdgate, G. A., Isothermal titration calorimetry in drug discovery. *Prog Med Chem* **2001,** *38*, 309-76.

49.   Pierce, M. M.; Raman, C. S.; Nall, B. T., Isothermal Titration Calorimetry of Protein–Protein Interactions. *Methods* **1999,** *19* (2), 213-221.

50.   Thomson, J. A.; Ladbury, J. E., Isothermal Titration Calorimetry: A Tutorial. In *Biocalorimetry 2*, 2004; pp 35-58.

51.   Huang, R.; Lau, B. L. T., Biomolecule–nanoparticle interactions: Elucidation of the thermodynamics by isothermal titration calorimetry. *Biochimica et Biophysica Acta (BBA) - General Subjects* **2016,** *1860* (5), 945-956.

52.   De, M.; You, C.-C.; Srivastava, S.; Rotello, V. M., Biomimetic Interactions of Proteins with Functionalized Nanoparticles: A Thermodynamic Study. *Journal of the American Chemical Society* **2007,** *129* (35), 10747-10753.

53.   Wang, X.; Matei, E.; Gronenborn, A. M.; Ramström, O.; Yan, M., Direct Measurement of Glyconanoparticles and Lectin Interactions by Isothermal Titration Calorimetry. *Analytical Chemistry* **2012,** *84* (10), 4248-4252.

54.   Srinivasan, K.; Parimal, S.; Lopez, M. M.; McCallum, S. A.; Cramer, S. M., Investigation into the Molecular and Thermodynamic Basis of Protein

Interactions in Multimodal Chromatography Using Functionalized Nanoparticles. *Langmuir* **2014,** *30* (44), 13205-13216.

55.   Peng, Y.; Shen, Y.; Ge, M.; Pan, Z.; Chen, W.; Gong, B., Efficient extraction of heavy metals from collagens by sulfonated polystyrene nanospheres. *Food Chemistry* **2019,** *275*, 377-384.

56.   Drout, R. J.; Kato, S.; Chen, H.; Son, F. A.; Otake, K.-I.; Islamoglu, T.; Snurr, R. Q.; Farha, O. K., Isothermal Titration Calorimetry to Explore the Parameter Space of Organophosphorus Agrochemical Adsorption in MOFs. *Journal of the American Chemical Society* **2020,** *142* (28), 12357-12366.

57.   Sahu, A.; Blackburn, K.; Durkin, K.; Eldred, T. B.; Johnson, B. R.; Sheikh, R.; Amburgey, J. E.; Poler, J. C., Green synthesis of nanoscale anion exchange resin for sustainable water purification. *Environmental Science: Water Research & Technology* **2018,** *4* (10), 1685-1694.

58.   Rathi, B. S.; Kumar, P. S., Electrodeionization theory, mechanism and environmental applications. A review. *Environmental Chemistry Letters* **2020,** *18* (4), 1209-1227.

59.   Wang, Y.; Wang, G. Y.; Moitessier, N.; Mittermaier, A. K., Enzyme Kinetics by Isothermal Titration Calorimetry: Allostery, Inhibition, and Dynamics. *Front. Mol. Biosci.* **2020,** *7*, 19.

60.   Choma, C. T. *Characterizing Binding Interactions by ITC*; TA Instruments: 109 Lukens Drive, New Castle, DE 19720, USA.

61.   Velázquez Campoy, A.; Freire, E., ITC in the post-genomic era...? Priceless. *Biophys Chem* **2005,** *115* (2-3), 115-24.

62.   Quinn, C. F. *Analyzing ITC Data for the Enthalpy of Binding Metal Ions to Ligands*; TA Instruments: 890 West 410 North, Lindon, UT 84042, USA.

63.   Feig, A., *Calorimetry*. Elsevier Science & Technology: San Diego, UNITED STATES, 2016.

64.   Kuo, T. C.; Lee, P. C.; Tsai, C. W.; Chen, W. Y., Salt bridge exchange binding mechanism between streptavidin and its DNA aptamer - thermodynamics and spectroscopic evidences. *J. Mol. Recognit.* **2013,** *26* (3), 149-159.

65.   Niether, D.; Sarter, M.; Konig, B.; Zamponi, M.; Fitter, J.; Stadler, A.; Wiegand, S., Thermodiffusion as a Probe of Protein Hydration for Streptavidin and the Streptavidin-Biotin Complex. In *Irago Conference 2017: A 360-Degree Outlook on Critical Scientific and Technological Challenges for a Sustainable Society*, Sandhu, A.; Sharma, J., Eds. Amer Inst Physics: Melville, 2018; Vol. 1929.

66.   Mpye, K. L.; Gildenhuys, S.; Mosebi, S., The effects of temperature on streptavidin-biotin binding using affinity isothermal titration calorimetry. *AIMS Biophys.* **2020,** *7* (4), 236-247.